# A Hybridized Discontinuous Galerkin Formulation for Modeling Electrohydrodynamic Thrusters

by

Andrew Dexter

Submitted to the Department of Aeronautics and Astronautics
in partial fulfillment of the requirements for the degree of

Master of Science

at the

MASSACHUSETTS INSTITUTE OF TECHNOLOGY

June 2015





Signature redacted

Author .....
Department of Aeronautics and Astronautics
May 14, 2015

Signature redacted

Certified by .....
Steven R.H. Barrett
Associate Professor
Thesis Supervisor

Signature redacted

Accepted by .....
Paulo C. Lozano
Associate Professor of Aeronautics and Astronautics
Chair, Graduate Program Committee

# A Hybridized Discontinuous Galerkin Formulation for Modeling Electrohydrodynamic Thrusters

by

Andrew Dexter

Submitted to the Department of Aeronautics and Astronautics
on May 14, 2015, in partial fulfillment of the
requirements for the degree of
Master of Science

## Abstract

Electrohydrodynamic (EHD) thrusters utilize ion neutral collisions in air to produce a propulsive force. The ions are generated at an emitting electrode in an asymmetric capacitor by a corona discharge. This thesis presents a Hybridized Discontinuous Galerkin (HDG) formulation for solving the EHD thruster governing equations with the exception of fluid flow equations. The problem is two-way coupled and non-linear. A smoothed charge injection model from the literature for the corona discharge is included in the HDG scheme. The formulation is validated against a model problem which has an analytical solution and parallel wire single stage and dual stage thruster performance data from the literature. The model problem consists of concentric cylinders with charge density and potential specified on the inner and outer cylinders. The inner cylinder is offset to test the charge injection boundary condition in an asymmetric solution. The single stage thruster consists of two parallel wires of different diameters separated by a 1 cm gap. The dual stage thruster consists of three inline parallel wires of different diameters separated by 1 cm and 3 cm. The HDG solution for the model problem is found to produce normalized errors on the order of $10^{-3}$ for the potential and charge density solutions. The charge density applied to the inner emitter electrode is increased over several solution iterations to resolve high charge density gradients. The charge density boundary condition applied to the offset case represented the expected qualities of a corona discharge. The smoothed boundary condition is shown to be tunable to allow for a trade-off between accuracy and numerical stability. The single stage thruster model replicated experimental thrust results within 14% error using homogeneous charge injection and the smoothed charge injection model requires a less stable setting to achieve similar accuracy. The dual stage model shows the necessity of a mixed outflow boundary condition to avoid non-unique solutions.

Thesis Supervisor: Steven R.H. Barrett
Title: Associate Professor

# Acknowledgments

I could not have completed this work without the support of my adviser, Steven Barrett, and advice from Paulo Lozano. Ngoc Cuong Nguyen's help with understanding and troubleshooting the HDG methodology and implementation has proven to be invaluable. I appreciate the computing resources and space provided by the Laboratory for Aviation and the Environment. My time at MIT would not be possible without support from GE Aviation. Finally, I would like to thank my wife and parents for their unfailing encouragement and patience.

# Contents


**1 Introduction and Theory** **15**

1.1 Corona Discharge . . . . . 17

1.2 Thrust Mechanism . . . . . 19

1.2.1 Governing Equations . . . . . 20

1.2.2 EHD Thrust Investigations . . . . . 20

**2 Previous Work on EHD Thruster Modeling** **23**

2.1 FEM/MOC Theory . . . . . 26

2.2 Model Problem . . . . . 27

**3 Numerical Formulation and Theory** **31**

3.1 Governing Equations . . . . . 31

3.2 HDG Formulation . . . . . 33

3.2.1 Function Spaces and Inner Products . . . . . 34

3.2.2 Weak Form . . . . . 35

3.2.3 Linearization . . . . . 36

3.3 Boundary Conditions . . . . . 38

3.3.1 Dirichlet Boundary Conditions . . . . . 39

3.3.2 Neumann Boundary Conditions . . . . . 40

3.4 Implementation . . . . . 42

3.4.1 Meshing . . . . . 42

3.4.2 Solving . . . . . 44

3.4.3 Post-Processing . . . . . 46

3.5 Validation Procedure . . . . . 46

**4 Results** **49**

4.1 Model Problem . . . . . 49

4.1.1 Approximation of Analytical Solution . . . . . 50

4.1.2 Determination of $\rho_{ref}$ and $E_{ref}$ . . . . . 54

4.1.3 Evaluation of Charge Injection Boundary Condition . . . . . 58

4.2 Single Stage Thruster . . . . . 64

4.3 Dual Stage Thruster . . . . . 73

**5 Conclusions** **75**

5.1 Recommendations for Future Work . . . . . 77

**A HDG for Poisson Equation** **79**

**B Sensitivity Functions** **81**

**C Integration Implementation** **85**

**D Analysis Meshes** **87**

# List of Figures


1-1 Single stage EHD thruster. . . . . 16

2-1 Concentric cylinders for model problem. . . . . 28

3-1 Fifth order DG element, nodes are shown with small perturbations to avoid overlaps. . . . . 44

3-2 Model problem solution for $r_a = 0.01\,\mathrm{m}$, $\rho_0 = 10^{-5}\,\mathrm{Cm}^{-3}$, and $\phi_0 = 5\,\mathrm{kV}$. 47

3-3 Dual stage thruster geometry. . . . . 48

4-1 Model problem normalized residuals for $r_a = 0.01\,\mathrm{m}$, $\rho_0 = 10^{-5}\,\mathrm{Cm}^{-3}$, and $\phi_0 = 5\,\mathrm{kV}$. . . . . 50

4-2 Plot of $\log\|e^{n+1}\|_{L^2}$ vs. $\log\|e^n\|_{L^2}$ for identical meshes with basis functions of order $k$. . . . . 51

4-3 Model problem solution for $r_a = 0.01\,\mathrm{m}$, $\rho_0 = 10^{-5}\,\mathrm{Cm}^{-3}$, and $\phi_0 = 5\,\mathrm{kV}$. 52

4-4 Scalar solution errors for $r_a = 0.01\,\mathrm{m}$, $\rho_0 = 10^{-5}\,\mathrm{Cm}^{-3}$, and $\phi_0 = 5\,\mathrm{kV}$. 52

4-5 Model problem solution for $r_a = 0.01\,\mathrm{m}$, $\rho_0 = 10^{-5}\,\mathrm{Cm}^{-3}$, and $\phi_0 = 5\,\mathrm{kV}$. 53

4-6 Maximum electric field vs. applied voltage for model problem with inner electrode offset by $r_b/2$, $\rho_0 = 0\,\mathrm{Cm}^{-3}$. . . . . 54

4-7 Maximum and minimum electric field strength on emitter surface as a function of charge density. . . . . 55

4-8 Potential solution for $V = 150\,\mathrm{kV}$. . . . . 56

4-9 Electric field and charge density solution for $V = 150\,\mathrm{kV}$, $\rho_0 = 1 \times 10^{-4}\,\mathrm{Cm}^{-3}$. 56

4-10 Charge density gradient and current density solution for $V = 150\,\mathrm{kV}$, $\rho_0 = 1 \times 10^{-4}\,\mathrm{Cm}^{-3}$. . . . . 57

4-11 Charge injection term from equation (3.5) (see table 4.2 for cases). . . 58
4-12 Charge density solution using charge injection boundary condition, $\phi_0 = 150\,\mathrm{kV}$. . . . . 59
4-13 Charge density and current density solution using charge injection boundary condition, $\rho_{ref} = 10^{-6}\,\mathrm{Cm}^{-3}$, $E_{ref} = 12.14\,^{\mathrm{kV}}/_{\mathrm{cm}}$, and $\phi_0 = 250\,\mathrm{kV}$. . . . . 60
4-14 Electric field, current density, and charge density along the emitter surface, $\phi_0 = 150\,\mathrm{kV}$ (see table 4.2 for cases). . . . . 62
4-15 Electric field, current density, and charge density along the emitter surface, $\rho_{ref} = 10^{-6}\,\mathrm{Cm}^{-3}$ and $E_{ref} = 12.14\,^{\mathrm{kV}}/_{\mathrm{cm}}$; cases correspond to $\phi_0 = 150\,\mathrm{kV}$, $200\,\mathrm{kV}$, and $250\,\mathrm{kV}$. . . . . 63
4-16 Charge density solution with charge injection boundary condition $\rho_{ref} = 10^{-5}\,\mathrm{Cm}^{-3}$ and $E_{ref} = 1\,^{\mathrm{kV}}/_{\mathrm{cm}}$ on the coarse mesh. . . . . 65
4-17 Solution using homogeneous charge injection boundary condition with $I_m = 0.46\,\mathrm{mA}$, $\phi_0 = 13\,\mathrm{kV}$. . . . . 66
4-18 Solution using charge injection boundary condition $\rho_{ref} = 10^{-4}\,\mathrm{Cm}^{-3}$ and $E_{ref} = 100\,^{\mathrm{kV}}/_{\mathrm{cm}}$, $\phi_0 = 13\,\mathrm{kV}$. . . . . 67
4-19 Thrust and current characteristics compared to experimental data and 1D theory. Experimental currents are applied to the emitter for the homogeneous case. Charge injection boundary condition cases: 1) $\rho_{ref} = 10^{-4}\,\mathrm{Cm}^{-3}$, $E_{ref} = 100\,^{\mathrm{kV}}/_{\mathrm{cm}}$, 2) $\rho_{ref} = 10^{-5}\,\mathrm{Cm}^{-3}$, $E_{ref} = 1\,^{\mathrm{kV}}/_{\mathrm{cm}}$ on coarse mesh, 3) $\rho_{ref} = 10^{-5}\,\mathrm{Cm}^{-3}$, $E_{ref} = 1\,^{\mathrm{kV}}/_{\mathrm{cm}}$ on fine mesh. . . . 68
4-20 Emitted and collected current for homogeneous boundary condition and charge injection boundary condition cases: 1) $\rho_{ref} = 10^{-4}\,\mathrm{Cm}^{-3}$, $E_{ref} = 100\,^{\mathrm{kV}}/_{\mathrm{cm}}$, 2) $\rho_{ref} = 10^{-5}\,\mathrm{Cm}^{-3}$, $E_{ref} = 1\,^{\mathrm{kV}}/_{\mathrm{cm}}$ on coarse mesh, 3) $\rho_{ref} = 10^{-5}\,\mathrm{Cm}^{-3}$, $E_{ref} = 1\,^{\mathrm{kV}}/_{\mathrm{cm}}$ on fine mesh. . . . . 69
4-21 Electric field strength, charge density, and current density on the emitter surface, $\phi_0 = 13\,\mathrm{kV}$. The charge injection settings are $\rho_{ref} = 10^{-4}\,\mathrm{Cm}^{-3}$, $E_{ref} = 100\,^{\mathrm{kV}}/_{\mathrm{cm}}$ and $\rho_{ref} = 10^{-5}\,\mathrm{Cm}^{-3}$, $E_{ref} = 1\,^{\mathrm{kV}}/_{\mathrm{cm}}$ for the high sensitivity case. . . . . 71

4-22 Electric field strength, charge density, and current density on the collector surface, $\phi_0 = 13\,\mathrm{kV}$. The charge injection settings are $\rho_{ref} = 10^{-4}\,\mathrm{Cm}^{-3}$, $E_{ref} = 100\,{}^{\mathrm{kV}}/_{\mathrm{cm}}$ and $\rho_{ref} = 10^{-5}\,\mathrm{Cm}^{-3}$, $E_{ref} = 1\,{}^{\mathrm{kV}}/_{\mathrm{cm}}$ for the high sensitivity case. . . . . 72

4-23 Un-converged potential and charge density solution using $\phi_0 = 5\,\mathrm{kV}$ and experimentally determined current 0.015 mA from Masuyama & Barrett [29,30]. . . . . 73

D-1 Model problem mesh, 1564 elements. . . . . 87

D-2 Model problem mesh with offset emitter, 1564 elements. . . . . 88

D-3 Single stage thruster mesh, 3746 elements. . . . . 88

D-4 Single stage thruster mesh, 11428 elements. . . . . 89

D-5 Dual stage thruster mesh, 2355 elements. . . . . 89

# List of Tables

1.1 Constants for Peek's law . . . . . 19

4.1 Error schedules for $\phi$ and $\rho$ showing convergence rate for each iteration, polynomial order $k = 2$. . . . . 51

4.2 Choices for $\rho_{ref}$ and $E_{ref}$ . . . . . 57

# Chapter 1

# Introduction and Theory

Advancements in aerial vehicles and propulsive technologies are only possible with concurrent development in engineering analysis tools. Development of high performance airplanes, unmanned aerial vehicles (UAV), and gas turbine engines have benefited from improvements in analysis tools such as Computational Fluid Dynamics (CFD) and Finite Element Method (FEM) techniques. Such tools are readily accessible through resources like openFOAM and the increasing power of personal computers. New developments in the field of electrohydrodynamics (EHD) geared towards feasible propulsion solutions for aerial vehicles necessitates the development of capable analysis tools and techniques.

EHD describes the behavior of fluids in the presence of electrostatic fields. The interaction of continuous media and electromagnetic fields is generally called continuum electromechanics. Melcher provides a detailed look at the governing principles including the coupling of Navier-Stokes (N-S) equations governing fluid flows and Maxwell's equations governing electromagnetic phenomenon [31, 32]. An EHD thruster is a device that uses electrostatic fields to affect a working fluid for the purpose of generating a propulsive thrust.

Recent work by Masuyama, Gilmore, and Barrett has shown that EHD thrusters may be of comparable efficiency to conventional means of propulsion in terms of thrust generated per unit power required [29, 30] and provides thrust density appropriate for small UAVs [16]. These investigations have been primarily theoretical and

experimental in nature with simple thruster geometries. Given the results of these efforts, the researchers aim to produce a proof of concept vehicle which uses an EHD thruster as the primary means of propulsion.

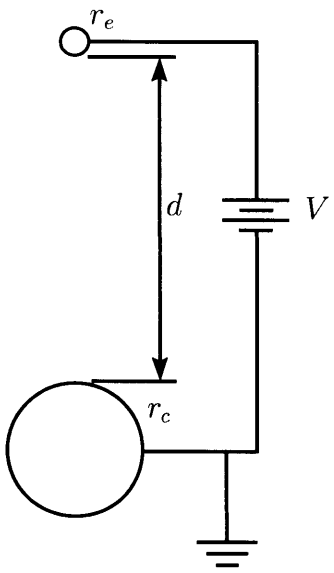


Figure 1-1: Single stage EHD thruster.

Figure 1-1 illustrates the basic EHD wire-to-cylinder thruster geometry which has been used in experimental studies [8, 16, 29, 30, 33, 51]. The configuration is an asymmetric capacitor where the electrodes are separated by a distance $d$ and the voltage difference $V$ between the electrodes is sufficiently high that a corona discharge is ignited at the smaller electrode which will be referred to as the emitter. The discharge ejects positive ions into the air gap between the electrodes. The ions are pulled towards towards the larger electrode, termed the collector, by electrostatic Coulomb forces given by

$$\vec{f_C} = \rho \vec{E}, \tag{1.1}$$

where $\vec{f_C}$ is the body force density, $\rho$ is the charge density in the air gap, and $\vec{E}$ is the electric field [19]. Ions undergo momentum transfer collisions with neutral species in the air gap resulting in flow which is termed the ionic or electric wind. The drift

velocity, $\vec{u}_D$, of the ions in the air gap is

$$\vec{u}_D = \mu \vec{E}, \tag{1.2}$$

where $\mu$ is the ion mobility in air which is $2.155 \times 10^{-4}\,\mathrm{m^2V^{-1}s^{-1}}$ for saturated air (100% RH) and $1.598 \times 10^{-4}\,\mathrm{m^2V^{-1}s^{-1}}$ for dry air [49]. The ion mobility is set to $2 \times 10^{-2}\,\mathrm{m^2V^{-1}s^{-1}}$ for this work. While the ion drift velocity is on the order of $100\,\mathrm{ms^{-1}}$, the ionic wind velocity has been measured in the lab at $1 - 10\%$ of the drift velocity [15, 33]. The ionic wind constitutes a net momentum flux and thus a net force on the device directed from the collector toward the emitter.

While the behavior and application of EHD thrusters have been characterized in the lab, the design of EHD thrusters has not been informed with application of modeling and analysis tools capable of assessing the impact of specific electrode geometries and configurations. A tool with predictive capabilities will be essential to the detailed design of air vehicles which take advantage of EHD thruster technology. This paper applies the Hybridized Discontinuous Galerkin (HDG) finite element method (FEM) to the EHD governing equations to develop a numerical scheme for modeling EHD thrusters. The remainder of this chapter will provide details of the governing physics and thrust mechanism. Previous work regarding modeling efforts will be discussed in chapter two. Chapter three presents the theoretical formulation and implementation of the HDG scheme. Results are reviewed in chapter four and discussed in chapter five.

## 1.1 Corona Discharge

In the presence of a high electric field near the emitter, free electrons gain sufficient energy for ionizing collisions with neutral air particles. The product electrons are free to undergo ionizing collisions as well while traveling to the positive electrode; positive ions migrate to the collector and recombine with electrons at the collector surface. The electron avalanches (Townsend discharge) are self-sustaining only where

the electric field strength is high enough that the electrons can be accelerated to sufficient energies for ionization collisions. The ionization region is thus confined to a zone very close to the emitter electrode [27]. This is known as a corona discharge since the electrode geometry strongly determines extent of the ionization region [17]. Thus far only a direct current (DC) unipolar positive corona discharge has been considered. The phenomenon is also observed for emitting electrodes of negative polarity or alternating polarity. The present numerical study is limited to a positive DC corona at the emitter.

The corona discharge, in addition to ejecting ions into the drift region, is also chemically active. The discharge produces ozone, molecular oxygen and nitrogen, and nitrogen oxides [5]. The discharge may also produce high energy electrons which can escape the device and radiation in the UV and x-ray spectrum [45].

The ignition or inception voltage, $V_0$, is the voltage at which a corona current is first observed. The ignition voltage is highly dependent on the electrode geometries of the EHD device since the minimum radius of curvature of the emitter electrode determines the maximum electric field. While the ionization processes at the emitter are best described via the kinetic theory of gases [3], experimental correlations have been determined to predict the macroscopic behavior of the corona discharge. Peek conducted a series of experiments to find the critical field strength resulting in the electrical breakdown of air as a function of the geometry of the emitting electrode and configuration of the device [41]. His studies were limited to geometries, like parallel or concentric cylinders, where the maximum electric field can be analytically calculated. The critical field strength varies according to

$$E_{crit} = E_0 m_s \delta \left(1 + \frac{c}{\sqrt{\delta r}}\right), \tag{1.3}$$

where $E_0$, $m_s$, and $c$ are experimentally determined constants and $r$ is the radius of the emitter wire in cm. This correlation is known as Peek's law or criterion. The parameter $\delta = 3.92P/T$, with pressure $P$ in cmHg and temperature $T$ in K, accounts for variation in atmospheric conditions. The electrode surface condition factor, $m_s$,

ranges from 0.67 to 1 for electrodes having surface irregularities like scratches or dirt. Peek recommended using $m_s = 0.87 - 0.9$ for general design purposes.

Table 1.1: Constants for Peek's law

| | $E_0[^{\text{kV}}/_{\text{cm}}]$ | $c$ |
|---|---|---|
| Parallel wires | 30 | .301 |
| Concentric cylinders | 31 | .308 |

Table 1.1 provides the remaining constants for Peek's law for parallel wires of equal radius and concentric cylinders. As voltage is increased after the inception of the corona discharge, the corona current is observed to increase according to the Townsend current-voltage relation $I \propto V(V - V_0)$ [6]. The positive corona current has a reducing effect on the max electric field on the emitter. Kaptsov's hypothesis is the assumption that the current pins the electric field at the emitter at the critical value [23]. Peek's law and Kaptsov's hypothesis provide a model of the electrostatic boundary condition at the surface of the emitter which can be used in numerical models.

## 1.2 Thrust Mechanism

While the ionic wind clearly results in a net momentum flux which manifests as thrusting force on the EHD device, the mechanism by which the force is applied to the device is less obvious. The charge distribution in the neutral fluid experiences Coulomb forces from the imposed electric field. By Newton's third law, the charge distribution must also act on the source of the electric field. Martins and Pinheiro investigated this hypothesis with numerical models and found that the electrostatic traction on the collector electrodes is primarily responsible for the EHD thrust [28].

### 1.2.1 Governing Equations

The macroscopic phenomena is described by three systems:

$$\rho_f \frac{D\vec{u}}{Dt} = -\nabla p + \vec{f_b} + \mu_v \nabla^2 \vec{u}, \tag{1.4a}$$

$$\nabla \cdot \vec{E} = \frac{\rho}{\epsilon_0}, \tag{1.4b}$$

$$\nabla \cdot \vec{j} = 0, \tag{1.4c}$$

where $\rho_f$ is the fluid density, $p$ is the pressure field, and $\mu_v$ is the fluid dynamic viscosity. For EHD thrusters the working fluid is air. Here (1.4a) is the incompressible Navier-Stokes equations, (1.4b) is Gauss's law, and (1.4c) enforces the conservation of charge. The primary unknowns in the system are fluid velocity $\vec{u}$, charge density $\rho$, and the electric field $\vec{E}$. The coupling mechanism between the fluid flow and electrostatic equations is the body force (see [14]) $\vec{f_b}$ which is given by

$$\vec{f_b} = \vec{f_C} = \rho \vec{E}. \tag{1.5}$$

The coupling is two-way since the fluid flow carries charge via advection given by $\rho\vec{u}$. The current density $\vec{j}$ is in general

$$\vec{j} = \rho(\mu \vec{E} + \vec{u}) - D\nabla\rho. \tag{1.6}$$

The other two terms, $\rho\mu\vec{E}$ and $-D\nabla\rho$, are ion drift due to the electric field and diffusion. The electric field drift term couples the charge conservation equation with Gauss's law and poses a challenge for numerical approaches to solving these equations since it is nonlinear. These issues will be addressed in more detail in chapters two and three.

### 1.2.2 EHD Thrust Investigations

The thrust produced by EHD devices has been characterized in a laboratory setting and compared against 1D theoretical analysis of (1.4). The primary findings are

summarized here. As stated earlier, the EHD thrust $T$ can be computed as the total Coulomb force on the emitted ions, which in 1D is

$$T = \frac{Id}{\mu}, \tag{1.7}$$

where $I$ is the total emitted current [16,29,30,42]. Gilmore & Barrett take this result a step further by using a streamtube analysis to show that (1.7) is true regardless of the impact of the charge distribution on the electric field [16]. Masuyama & Barrett [30] did note that the thrust deviates from the linear relation at higher applied voltages. The observed behavior is approximately bilinear for electrode gaps less than 15 cm and nonlinear for larger gaps. They posited that an electron current discharge at the collector electrode could account for the reduced performance. This is consistent with the behavior of corona discharges since high applied voltages induce streamers and sparks extending from the emitter to collector; these are concentrated current pathways with reduced interaction between the ions and the neutral media [26].

Since the corona current varies with voltage per the Townsend current-voltage relation, the thrust also varies with applied voltage $V$ as

$$T = \frac{CV(V - V_0)d}{\mu}, \tag{1.8}$$

where $C$ is a geometry dependent constant [6,29]. Since the input power to the device is simply $P = IV$, a thruster performance parameter is

$$\frac{T}{P} = \frac{Id}{\mu IV} = \frac{d}{\mu V}. \tag{1.9}$$

Thrust per input power is a measure of the thruster efficiency and increases as $V$ approaches $V_0$. While the thrust per power efficiency parameter has been shown by experiment to be comparable to established means of propulsion [29,30], the achievable thrust density may limit the application of EHD devices. Pekker & Young identified space charge limited (SCL) currents as a physical limitation of an EHD thruster and note that the performance of such a device will degrade with altitude

due to the reduction in air density [42]. They used a theoretical 1D thruster model to also conclude that the maximum thrust density cannot exceed $20\,\mathrm{Nm}^{-2}$ to $30\,\mathrm{Nm}^{-2}$. Wilson [51] conducted a series of experiments using various electrode shapes hoping to achieve a thrust density of $20\,\mathrm{Nm}^{-2}$. Though he failed in that goal, he did note that the configurations which resulted in more current draw and hence more thrust did not have the sharpest emitter electrodes. This implies that increasing the emitting surface area may also increase thrust.

The presence of a charge distribution in the space between electrodes (space charge) raises the potential in the gap and will eventually reduce the electric field to zero at the charge injection point. The current which causes this condition is the SCL current and varies as

$$I_{SCL} \propto V^{\frac{3}{2}}, \tag{1.10}$$

which is the well known Child-Langmuir law [25]. This effect is observed in ion thruster space propulsion devices. Gilmore & Barrett [16] take this concept into account and derive a theoretical max thrust density for a 1D EHD thruster which is given by

$$\frac{F}{A} = \frac{9}{8}\epsilon_0 \lambda \frac{V^2}{d^2}. \tag{1.11}$$

Gilmore & Barrett concluded their investigation by finding that the demonstrated thrust density may be suitable for a small unmanned aerial vehicle (UAV).

# Chapter 2

# Previous Work on EHD Thruster Modeling

Techniques for modeling the field and space charge due to a corona discharge have been developed for many different applications including electrostatic precipitators (ESP) [1,10,35,48,53], cooling for electronics [4], high voltage DC (HVDC) transmission lines [9], and thrusters [27,28]. The Continuous Galerkin (CG) FEM is commonly used since it provides flexibility for handling different geometries and commercial codes like FEMLAB, COMSOL, FLUENT, and ANSYS are available. Implementations of the CG method vary in the treatment of boundary conditions and handling of the corona charge injection phenomenon. Further, there are only few examples in the literature where the electrostatic equations are solved concurrently with the charge transport and fluid equations.

ESPs differ from EHD thrusters in that the unipolar current generated by the corona discharge is primarily used to charge and extract particulates or contaminants that are present in a fluid flow rather than generating thrust. The numerical techniques used for their analysis, however, are identical. Adamiak's review of simulation methods for wire-plate ESPs reveals that numerical approaches are limited to finite difference methods (FDM), CG-FEM, and the Finite Volume Method (FVM). A number of investigations included solution of the turbulent N-S equations [1]. The typical approach is to solve the electrostatic and charge transport equations sepa-

rately and pass the solution as a body force to a flow solver [52, 53]. There are few formulations that solve coupled flow, charge transport, and electrostatic systems concurrently; Skodras implemented a simultaneous solver for all three systems with user defined functions in FLUENT, which is a FVM based code, and Feng achieved a similar result by applying the standard CG-FEM [14, 15, 48].

While FVM and CG-FEM can successfully solve the pertinent equations, the use of Discontinuous Galerkin (DG) methods may overcome the shortcomings of each approach. DG methods are in a sense a generalization of the FVM in that they are locally conservative and the elements in the domain are connected by fluxes through element boundaries; the solution values can thus be discontinuous from element to element. DG methods, however, have the advantage of allowing high order representation of the solution within individual elements and thus are better able to handle large gradients in the solution [50]. DG methods are also more stable compared to CG-FEM formulations for convection-dominated problems [36,43]. The present problem is such a case; the dominating term in the current conservation equation is the ion drift due to the influence of the electric field. While Feng [13] argued that oscillations in the numerical solution are avoided by the application of Neumann boundary conditions at collector electrodes, the presented examples did not include freestream flow which would be present for an EHD thruster; large freestream velocities could impact solution stability with the CG-FEM approach. Further, the implementation of the charge injection boundary condition using Kaptsov's hypothesis required addition of additional residual equations which would result in oscillations if the feedback term was not selected appropriately [13].

The primary criticism of DG-FEM is that the method is too computationally expensive since they require degrees of freedom on element boundaries in addition to degrees of freedom on the element interior. The Multiscale DG (MDG) [22] and Embedded DG (EDG) [18] methods address this problem by considering the solution on element boundaries as the set of global unknowns. However, MDG and EDG are not locally conservative and have similar convergence rates compared to CG-FEM [36].

The HDG method - first introduced for elliptic problems by Cockburn, Gopalakrishnan, & Lazarov [7] - constitutes an improvement over MDG and EDG in that the solution is locally conservative and displays optimal convergence rates for all approximate variables while remaining competitive with CG-FEM in terms of computational efficiency [36]. Nguyen & Peraire show HDG formulations for a number of different problem types in fluid dynamics and solid mechanics and note that the generality of the HDG approach allows it to be readily adapted for other PDE systems including electromagnetics [36, 40] .

While DG methods have clear advantages for problems in computational fluid dynamics and have been applied to problems in linear elasticity, Maxwell equations, and plates [2, 40]. Application to EHD equations have been limited. Vázquez & Castellanos applied an upwinded DG method to the charge transport equation while relying on CG-FEM for solving the electrostatic and fluid flow systems for transient charge injection between parallel plates [50]. They used a simple cut-off scheme to deal with non-physical negative values of electric charge which result from high gradients; application of a complex slope limiter would yield more consistent results. They noted that the upwinding results in a more diffusive solution compared to Particle-in-Cell (PIC) or Method of Characteristics (MOC) results; a diffusion term was not included in the formulation. Overall, Vázquez & Castellanos concluded favorably for applying DG methods to the charge transport equation due to the high accuracy of the steady state solution and ease of implementation compared to the PIC method.

Tools for analyzing EHD thrusters using FVM and CG-FEM have already been developed but suffer from the shortcomings of each numerical scheme. HDG formulations for a variety of flow systems have already been developed but have not been coupled to the electrostatic and charge transport systems. Given the proven advantages of the HDG approach and a need for a predictive analysis tool for EHD thrusters, application of the HDG method to the electrostatic and charge transport equation is a worthwhile endeavor and the first step in developing a tool for analyzing all aspects of an EHD thruster.

## 2.1 FEM/MOC Theory

This section illustrates some of the difficulty in simultaneously solving the electrostatic and charge transport equations by looking at the CG-FEM/MOC approach for these equations. By only considering the drift due to the electric field, equations (1.4) can be reduced to

$$\nabla^2\phi = -\frac{\rho}{\epsilon_0}, \tag{2.1}$$

$$\mu\nabla\phi\cdot\nabla\rho = \frac{\mu\rho^2}{\epsilon_0}. \tag{2.2}$$

The equations exhibit two-way coupling through $\phi$ and $\rho$ with a nonlinear term in equation (2.2). While equation (2.1) is the familiar elliptic Poisson problem and is readily solved using CG-FEM if $\rho$ is known, equation (2.2) has a form that is suitable for the Method of Characteristics (MOC) technique [9]. Equation (2.2) has characteristic curves given by

$$\frac{dx}{dt} = -\mu\frac{d\phi}{dx}, \tag{2.3a}$$

$$\frac{dy}{dt} = -\mu\frac{d\phi}{dy}. \tag{2.3b}$$

Given a solution for $\phi$, the charge density along any characteristic line can be calculated by solving

$$\frac{d\rho}{dt} = -\frac{\mu\rho^2}{\epsilon_0}. \tag{2.4}$$

Equation (2.4) can be integrated in time to yield

$$\rho(t) = \left[\frac{1}{\rho_0} + \left(\frac{\mu}{\epsilon_0}\right)t\right]^{-1}. \tag{2.5}$$

The system given by (2.1) and (2.2) can then be fully solved by following the procedure:

1. Solve equation (2.1) with $\rho = 0$ over the domain.
2. Guess $\rho_0$ at the emitter surface.

3. Calculate characteristic trajectories and space charge distribution using (2.3) and (2.5).
4. Solve equation (2.1) with $\rho$ from step 3.
5. Iterate on steps 3 and 4 until $\phi$ and $\rho$ are converged.
6. Check that the electric field on the emitter surface meets any applied criteria e.g. Peek's law.
7. If step 6 is not satisfied, update $\rho_0$ and return to step 3.

While solution of the equations in the above manner is relatively straightforward, there are aspects of the implementation which pose significant difficulties, particularly if a flexible analysis tool is desired. The characteristic trajectories must be calculated in time which requires the use of algorithms like adaptive Runge-Kutta [11] in order to ensure the step size guarantees a certain level of accuracy. The error in the trajectory increases the longer equations (2.3) are integrated. Given the small size of the emitter relative to the domain, the step size must be very fine in the vicinity of the emitter to ensure the trajectory does not bypass the emitter. This problem is made worse by the high electric field strength near the emitter. In addition to the problems with time integration, a sufficient number of trajectories must be calculated to ensure sufficient coverage of the domain. These problems require an implementation that is very specific to a given EHD thruster geometry. The routines which calculate trajectories must be tailored for each thruster and perhaps for a given set of boundary conditions. This underscores the need for an approach which allows simultaneous solution of the governing equations.

## 2.2 Model Problem

Validation of the HDG implementation and assessment of convergence rates requires an analytical solution. The simplest geometry to validate the implementation is concentric cylinders as shown in figure 2-1. While general analytic solutions for this geometry are complex (see [12]), a simple analytical solution is possible by assuming a constant electric field. It is clear from the geometry that the solution is axisymmetric

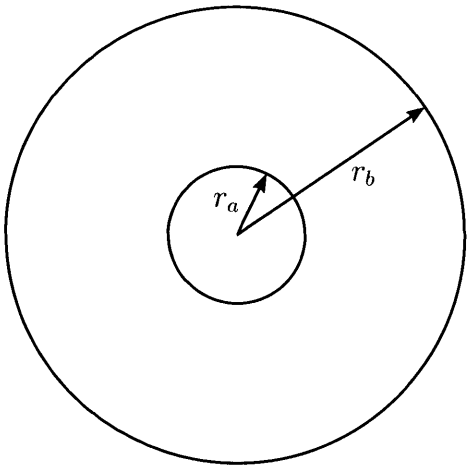


Figure 2-1: Concentric cylinders for model problem.

as long as the boundary conditions are homogeneous. Given these assumptions, the governing equations in cylindrical coordinates are

$$E_r + \frac{\partial \phi}{\partial r} = 0, \tag{2.6a}$$

$$\frac{1}{r}\frac{\partial (rE_r)}{\partial r} = \frac{\rho}{\epsilon_0}, \tag{2.6b}$$

$$\frac{1}{r}\frac{\partial (r\mu\rho E_r)}{\partial r} = 0, \tag{2.6c}$$

where $E_r$ is the radial component of the electric field. Substituting (2.6a) into (2.6b) and (2.6c) and taking the derivative yields

$$\frac{1}{r}\frac{\partial \phi}{\partial r} + \frac{\partial^2 \phi}{\partial r^2} = -\frac{\rho}{\epsilon_0}, \tag{2.7a}$$

$$\mu\rho \underbrace{\left(\frac{1}{r}\frac{\partial \phi}{\partial r} + \frac{\partial^2 \phi}{\partial r^2}\right)}_{-\rho/\epsilon_0} + \mu \frac{\partial \rho}{\partial r}\frac{\partial \phi}{\partial r} = 0. \tag{2.7b}$$

Simplifying (2.7b) further results in

$$-\frac{\rho^2}{\epsilon_0} + \frac{\partial \rho}{\partial r}\frac{\partial \phi}{\partial r} = 0. \tag{2.8}$$

If $E_r$ is constant, the potential $\phi$ will be linear in $r$ with the assumed form

$$\phi(r) = A(r - B) + C, \tag{2.9}$$

where $A$, $B$, and $C$ are constants to be determined. If $\phi_0$ is the potential at the inner cylinder, $r = r_a$, then

$$\phi(r) = A(r - r_a) + \phi_0. \tag{2.10}$$

Using (2.10) in (2.7a) and defining $\rho(r_a) = \rho_0$, then

$$\phi(r) = -\frac{r_a \rho_0}{\epsilon_0}(r - r_a) + \phi_0, \tag{2.11a}$$

$$E_r = -\frac{\partial \phi}{\partial r} = \frac{r_a \rho_0}{\epsilon_0}. \tag{2.11b}$$

Now a suitable equation for $\rho(r)$ is found by inspection after substituting (2.11a) into (2.8). The charge density is then given by

$$\rho(r) = \frac{r_a \rho_0}{r}. \tag{2.12}$$

The boundary conditions on the outer cylinder, $r = r_b$, have not yet been considered. The assumption that $E_r$ is constant over the domain precludes specification of another boundary condition on the outer cylinder. A numerical boundary value problem requires specification of an additional boundary condition to ensure that the solution is unique. Requiring $\phi(r_b) = 0$ determines the geometry of the outer cylinder. Using the boundary condition in (2.11a) and solving for $r_b$ yields

$$r_b = \frac{\phi_0 \epsilon_0}{r_a \rho_0} + r_a. \tag{2.13}$$

The analytical solution and geometry of the outer cylinder are fully defined if $\rho_0$, $r_a$, and $\phi_0$ are specified.

# Chapter 3

# Numerical Formulation and Theory

This chapter develops an HDG-FEM scheme for solving the governing equations for an EHD thruster. The N-S equations are not considered in this formulation since HDG schemes have already been developed by Nguyen & Peraire [36]. Since modeling steady state performance of a thruster is of interest, all time dependent terms in the formulation are zero. The governing equations are presented and developed into a weak form using HDG methods. Finally boundary conditions and aspects of the numerical implementation are discussed.

## 3.1 Governing Equations

The simplest EHD thruster consists of a unipolar corona discharge at an emitting electrode and a downstream collecting electrode. The relationship between the electric field, $\vec{E}$, and charge density, $\rho$, is described by Gauss's Law

$$\nabla \cdot \vec{E} = \frac{\rho}{\epsilon_0}, \tag{3.1}$$

where $\epsilon_0 \approx 8.854 \times 10^{-12}\,{}^{\mathrm{F}}/_{\mathrm{m}}$ is the permittivity of free space. Equation (3.1) is valid for an EHD thruster in air since the relative permittivity of air is approximately one [21]. Given that the system is at steady state, the Maxwell-Faraday equation

gives

$$\nabla \times \vec{E} = -\frac{\partial \vec{B}}{\partial t} = 0. \tag{3.2}$$

This allows the electric field to be defined as

$$\vec{E} = -\nabla\phi, \tag{3.3}$$

where $\phi$ is the electric potential. Conservation of charge requires that

$$\nabla \cdot \vec{j} = 0. \tag{3.4}$$

The current density, $\vec{j}$, has contributions from electric field drift, advection, and diffusion and is expressed as

$$\vec{j} = \rho(\mu\vec{E} + \vec{u}) - D\nabla\rho \tag{3.5}$$

where $\mu$ is the ion mobility in air, $\vec{u}$ is the velocity field, and $D$ is the diffusivity of charged particles in air. $D$ is related to the ambient temperature, $T$, and elementary charge, $q \approx 1.602 \times 10^{-19}\,\mathrm{C}$, by Einstein's relation

$$D = \frac{\mu k_B T}{q}, \tag{3.6}$$

where $k_B \approx 1.3806 \times 10^{-23}\,{}^{\mathrm{J}}/_{\mathrm{K}}$ is the Boltzmann constant. The governing equations are simplified by ignoring the advection component of the current density. Determination of the fluid velocity field via the N-S equations is beyond the scope of the current work. Further, the electrostatically induced velocity has been found to typically be less than 10% of the ion drift velocity [15]. The field drift term remains the primary component of current density. The diffusion term may also be ignored given that the coefficient $D$ is on the order of $10^{-6}$ whereas the drift term is on the order $10^1 - 10^2$. Though other numerical schemes have made both simplifying assumptions [9, 13], ignoring diffusion in the HDG formulation leads to a matrix system which is singular for the trivial solution where all variables are zero.

The final system of governing equations is the following:

$$\vec{E} + \nabla\phi = 0, \tag{3.7}$$

$$\vec{C} + \nabla\rho = 0, \tag{3.8}$$

$$\nabla \cdot \vec{E} = \frac{\rho}{\epsilon_0}, \tag{3.9}$$

$$\nabla \cdot (D\vec{C} + \mu\rho\vec{E}) = 0. \tag{3.10}$$

Here $\vec{C}$ is introduced as the gradient of $\rho$ such that the equations can be expressed as follows:

$$\boldsymbol{Q} + \nabla\boldsymbol{u} = 0, \tag{3.11}$$

$$-\nabla \cdot \boldsymbol{F}(\boldsymbol{Q}, \boldsymbol{u}) + \boldsymbol{s}(\boldsymbol{u}) = 0, \tag{3.12}$$

where

$$\boldsymbol{Q} = \begin{pmatrix} \vec{E} \\ \vec{C} \end{pmatrix} \qquad \boldsymbol{u} = \begin{pmatrix} \phi \\ \rho \end{pmatrix} \tag{3.13}$$

$$\boldsymbol{F} = \begin{pmatrix} \vec{E} \\ D\vec{C} + \mu\rho\vec{E} \end{pmatrix} \qquad \boldsymbol{s} = \begin{pmatrix} \frac{\rho}{\epsilon_0} \\ 0 \end{pmatrix} \tag{3.14}$$

The field drift term, $\mu\rho\vec{E}$, in equation (3.10) introduces nonlinearity into the problem. The equations are also coupled since the source term for equation (3.9) is a function of the solution to equation (3.10). Any numerical scheme to solve these equations must have a suitable linearization approach.

## 3.2 HDG Formulation

DG-FEM methods allow the approximate solution to be discontinuous across element boundaries. This leads to increases in problem degrees of freedom since there are repeated nodes at element boundaries. The HDG method is a refinement of the DG

approach in that the problem is solved only using degrees of freedom on the element boundaries. This is accomplished through appropriate choice of function spaces and introduction of independent variables on element boundaries which approximate the numerical trace of the solution. In many cases, the HDG approach is competitive with CG-FEM schemes in terms of computational efficiency and accuracy [36]. The application of HDG methods to the present problem closely follows techniques presented by Nguyen et al. [36–38].

### 3.2.1 Function Spaces and Inner Products

A finite physical domain, $\Omega$, in $\mathbb{R}^d$ with boundaries $\partial\Omega$ is discretized by a set of disjoint elements denoted by $\mathcal{T}_h$. A given element in the set $\mathcal{T}_h$ is called $K$. $\partial\Omega$ is the union of $\partial\Omega_D$ and $\partial\Omega_N$ which denote boundaries where Dirichlet and Neumann boundary conditions are applied. Note that $\partial\Omega_D \cap \partial\Omega_N = \emptyset$. The set $\partial\mathcal{T}_h = \{\partial K : K \in \mathcal{T}_h\}$ consists of all element boundaries in $\mathcal{T}_h$. Each element boundary $\partial K$ has an outward unit normal $\boldsymbol{n}$. The set of element faces $\partial K$ on the domain boundary $\partial\Omega$ is denoted $\mathcal{E}_h^0$ and any individual face is called $F$. $\mathcal{E}_h^\partial$ is the set of faces shared by any two elements, $K^+$ and $K^-$, in $\mathcal{T}_h$. The full set of faces $\mathcal{E}_h$ is the union of boundary and interior faces, $\mathcal{E}_h^0$ and $\mathcal{E}_h^\partial$. The difference between $\partial\mathcal{T}_h$ and $\mathcal{E}_h$ is that $\mathcal{E}_h$ contains each face in the domain once whereas interior faces are repeated in $\partial\mathcal{T}_h$.

The set of function spaces necessary for the discontinuous finite element projection are

$$
\begin{aligned}
\mathcal{W}_h^k &= \{a \in L^2(\mathcal{T}_h) : a|_K \in \mathcal{P}^k(K), \forall K \in \mathcal{T}_h\},\\
\boldsymbol{\mathcal{V}}_h^k &= \{\boldsymbol{a} \in (L^2(\mathcal{T}_h))^m : \boldsymbol{a}|_K \in (\mathcal{P}^k(K))^m, \forall K \in \mathcal{T}_h\},\\
\boldsymbol{\mathcal{Q}}_h^k &= \{\boldsymbol{A} \in (L^2(\mathcal{T}_h))^{m\times d} : \boldsymbol{A}|_K \in (\mathcal{P}^k(K))^{m\times d}, \forall K \in \mathcal{T}_h\},\\
\boldsymbol{\mathcal{M}}_h^k &= \{\boldsymbol{\mu} \in (L^2(\mathcal{E}_h))^m : \boldsymbol{\mu}|_F \in (\mathcal{P}^k(F))^m, \forall F \in \mathcal{E}_h\}.
\end{aligned}
$$

$\mathcal{P}^k(\omega)$ are polynomials of degree $k$ defined over a domain $\omega$. Functions associated

with the element spaces have components as follows for $1 \leq i \leq m$ and $1 \leq j \leq d$:

$$\boldsymbol{a} = (a_i),$$
$$\boldsymbol{A} = (A_{ij}),$$
$$\boldsymbol{\mu} = (\mu_i).$$

All functions except those belonging to $\boldsymbol{\mathcal{M}}_h^k$ are square integrable in the domain and are discontinuous between elements; functions in $\boldsymbol{\mathcal{M}}_h^k$ are only integrable along faces and are discontinuous between faces. The following volume inner products can now be defined:

$$(a,b)_{\mathcal{T}_h} = \sum_{K\in\mathcal{T}_h} (a,b)_K, \text{ where } (a,b)_K = \int_K ab,$$
$$(\boldsymbol{a},\boldsymbol{b})_{\mathcal{T}_h} = \sum_{K\in\mathcal{T}_h} (\boldsymbol{a},\boldsymbol{b})_K, \text{ where } (\boldsymbol{a},\boldsymbol{b})_K = \int_K \boldsymbol{a}\cdot\boldsymbol{b}, \text{ and}$$
$$(\boldsymbol{A},\boldsymbol{B})_{\mathcal{T}_h} = \sum_{K\in\mathcal{T}_h} (\boldsymbol{A},\boldsymbol{B})_K, \text{ where } (\boldsymbol{A},\boldsymbol{B})_K = \int_K \mathrm{tr}(\boldsymbol{A}^{\mathrm{T}}\boldsymbol{B}).$$

There are also corresponding boundary inner products as follows:

$$\langle a,b\rangle_{\partial\mathcal{T}_h} = \sum_{\partial K\in\partial\mathcal{T}_h} \langle a,b\rangle_{\partial K}, \text{ where } \langle a,b\rangle_{\partial K} = \int_{\partial K} ab,$$
$$\langle \boldsymbol{a},\boldsymbol{b}\rangle_{\partial\mathcal{T}_h} = \sum_{\partial K\in\partial\mathcal{T}_h} \langle \boldsymbol{a},\boldsymbol{b}\rangle_{\partial K}, \text{ where } \langle \boldsymbol{a},\boldsymbol{b}\rangle_{\partial K} = \int_{\partial K} \boldsymbol{a}\cdot\boldsymbol{b}, \text{ and}$$
$$\langle \boldsymbol{A},\boldsymbol{B}\rangle_{\partial\mathcal{T}_h} = \sum_{\partial K\in\partial\mathcal{T}_h} \langle \boldsymbol{A},\boldsymbol{B}\rangle_{\partial K}, \text{ where } \langle \boldsymbol{A},\boldsymbol{B}\rangle_{\partial K} = \int_{\partial K} \mathrm{tr}(\boldsymbol{A}^{T}\boldsymbol{B}).$$

### 3.2.2 Weak Form

Manipulation of equations (3.11) and (3.12) to a weak form is accomplished by multiplying through with test functions and integrating by parts. Approximate variables are introduced and denoted with the subscript $h$. The HDG formulation seeks an

approximation $(\boldsymbol{Q}_h, \boldsymbol{u}_h, \hat{\boldsymbol{u}}_h) \in \boldsymbol{\mathcal{Q}}_h^k \times \boldsymbol{\mathcal{V}}_h^k \times \boldsymbol{\mathcal{M}}_h^k$ such that

$$(\boldsymbol{Q}_h, \boldsymbol{A})_{\mathcal{T}_h} - (\boldsymbol{u}_h, \nabla \cdot \boldsymbol{A})_{\mathcal{T}_h} + \langle \hat{\boldsymbol{u}}_h, \boldsymbol{A} \cdot \boldsymbol{n} \rangle_{\partial \mathcal{T}_h} = 0, \tag{3.15}$$

$$(\boldsymbol{F}_h, \nabla \boldsymbol{a})_{\mathcal{T}_h} - \left\langle \hat{\boldsymbol{F}}_h \cdot \boldsymbol{n}, \boldsymbol{a} \right\rangle_{\partial \mathcal{T}_h} + (\boldsymbol{s}, \boldsymbol{a})_{\mathcal{T}_h} = 0, \tag{3.16}$$

$$\left\langle \hat{\boldsymbol{F}}_h \cdot \boldsymbol{n}, \boldsymbol{\mu} \right\rangle_{\partial \mathcal{T}_h} - \langle \boldsymbol{g}_N, \boldsymbol{\mu} \rangle_{\partial \Omega_N} = 0, \tag{3.17}$$

for all $(\boldsymbol{A}, \boldsymbol{a}, \boldsymbol{\mu}) \in \boldsymbol{\mathcal{Q}}_h^k \times \boldsymbol{\mathcal{V}}_h^k \times \boldsymbol{\mathcal{M}}_h^k$. Equation (3.17) enforces the continuity of fluxes through the domain and the Neumann boundary conditions, $\boldsymbol{g}_N$, applied to $\partial \Omega_N$. The approximate numerical flux is

$$\hat{\boldsymbol{F}}_h = \boldsymbol{F}(\boldsymbol{Q}_h, \hat{\boldsymbol{u}}_h) - \tau(\boldsymbol{u}_h - \hat{\boldsymbol{u}}_h)\boldsymbol{n}, \tag{3.18}$$

where $\tau$ is a stabilization parameter with implications for solution stability and accuracy, particularly for convection dominated problems. Nguyen, Peraire, & Cockburn [37,38] provide a thorough analysis of the stability parameter and provide conditions that the parameter must meet. The present system can be solved by setting $\tau = 1$ for the electric field flux and $\tau = 1/D$ for the current density flux. This corresponds to a centered scheme for the fluxes. A more rigorous choice of $\tau$ may improve the solution convergence rate.

Dirichlet boundary conditions are applied by requiring $\hat{\boldsymbol{u}}_h = \boldsymbol{g}_D$ on $\partial \Omega_D$. After the system is linearized as shown in the following section, the Dirichlet conditions can be included in the initial solution and carried through each iteration by eliminating stiffness matrix rows and columns that correspond to degrees of freedom on $\partial \Omega_D$. Further details are provided in sections 3.3.1 and 3.4.

### 3.2.3 Linearization

The system of equations presented in section 3.2.2 cannot be solved implicitly due to the nonlinearity in the numerical flux. Newton's method is used to linearize the equations such that solution perturbations are calculated which reduce residuals from equations (3.15), (3.16), and (3.17). Given an approximate solution at the current

iterative step $n$, the solution at the $n+1$ step is defined by

$$\begin{aligned}
\boldsymbol{Q}_h^{n+1} &= \boldsymbol{Q}_h^n + \delta\boldsymbol{Q}_h^n, \\
\boldsymbol{u}_h^{n+1} &= \boldsymbol{u}_h^n + \delta\boldsymbol{u}_h^n, \\
\hat{\boldsymbol{u}}_h^{n+1} &= \hat{\boldsymbol{u}}_h^n + \delta\hat{\boldsymbol{u}}_h^n.
\end{aligned} \tag{3.19}$$

Solution dependent functions are defined in terms of the solution and solution perturbations at step $n$ by

$$\begin{aligned}
\boldsymbol{F}_h^{n+1} &= \boldsymbol{F}_h^n(\boldsymbol{Q}_h^n, \boldsymbol{u}_h^n) + \frac{\partial \boldsymbol{F}}{\partial \boldsymbol{Q}}(\boldsymbol{Q}_h^n, \boldsymbol{u}_h^n)\delta\boldsymbol{Q}_h + \frac{\partial \boldsymbol{F}}{\partial \boldsymbol{u}}(\boldsymbol{Q}_h^n, \boldsymbol{u}_h^n)\delta\boldsymbol{u}_h, \\
\hat{\boldsymbol{F}}_h^{n+1} &= \hat{\boldsymbol{F}}_h^n(\boldsymbol{Q}_h^n, \boldsymbol{u}_h^n, \hat{\boldsymbol{u}}_h^n) + \frac{\partial \hat{\boldsymbol{F}}}{\partial \boldsymbol{Q}}(\boldsymbol{Q}_h^n, \boldsymbol{u}_h^n, \hat{\boldsymbol{u}}_h^n)\delta\boldsymbol{Q}_h \\
&\qquad + \frac{\partial \hat{\boldsymbol{F}}}{\partial \boldsymbol{u}}(\boldsymbol{Q}_h^n, \boldsymbol{u}_h^n, \hat{\boldsymbol{u}}_h^n)\delta\boldsymbol{u}_h + \frac{\partial \hat{\boldsymbol{F}}}{\partial \hat{\boldsymbol{u}}}(\boldsymbol{Q}_h^n, \boldsymbol{u}_h^n, \hat{\boldsymbol{u}}_h^n)\delta\hat{\boldsymbol{u}}_h, \\
\boldsymbol{s}^{n+1} &= \boldsymbol{s}^n(\boldsymbol{u}_h^n) + \frac{\partial \boldsymbol{s}}{\partial \boldsymbol{u}}(\boldsymbol{u}_h^n)\delta\boldsymbol{u}_h, \\
\boldsymbol{g}_N^{n+1} &= \boldsymbol{g}_N^n + \frac{\partial \boldsymbol{g}_N}{\partial \boldsymbol{Q}}(\boldsymbol{Q}_h^n, \boldsymbol{u}_h^n)\delta\boldsymbol{Q}_h + \frac{\partial \boldsymbol{g}_N}{\partial \boldsymbol{u}}(\boldsymbol{Q}_h^n, \boldsymbol{u}_h^n)\delta\boldsymbol{u}_h.
\end{aligned} \tag{3.20}$$

Note that the Neumann boundary condition $\boldsymbol{g}_N$ can in general be nonlinear and a function of the solution. Substituting (3.19) and (3.20) into equations (3.15), (3.16), and (3.17) results in the following problem: find $(\delta\boldsymbol{Q}_h, \delta\boldsymbol{u}_h, \delta\hat{\boldsymbol{u}}_h) \in \boldsymbol{\mathcal{Q}}_h^k \times \boldsymbol{\mathcal{V}}_h^k \times \boldsymbol{\mathcal{M}}_h^k$ such that

$$a(\delta\boldsymbol{Q}_h, \boldsymbol{A}) + b(\delta\boldsymbol{u}_h, \boldsymbol{A}) + c(\delta\hat{\boldsymbol{u}}_h, \boldsymbol{A}) = n(\boldsymbol{A}), \tag{3.21}$$

$$h(\delta\boldsymbol{Q}_h, \boldsymbol{a}) + d(\delta\boldsymbol{u}_h, \boldsymbol{a}) + e(\delta\hat{\boldsymbol{u}}_h, \boldsymbol{a}) = f(\boldsymbol{a}), \tag{3.22}$$

$$k(\delta\boldsymbol{Q}_h, \boldsymbol{\mu}) + l(\delta\boldsymbol{u}_h, \boldsymbol{\mu}) + m(\delta\hat{\boldsymbol{u}}_h, \boldsymbol{\mu}) = g(\boldsymbol{\mu}), \tag{3.23}$$

for all $(\boldsymbol{A}, \boldsymbol{a}, \boldsymbol{\mu}) \in \boldsymbol{\mathcal{Q}}_h^k \times \boldsymbol{\mathcal{V}}_h^k \times \boldsymbol{\mathcal{M}}_h^k$ with forms given by

$$
\begin{aligned}
a(\delta\boldsymbol{Q}_h, \boldsymbol{A}) &= (\delta\boldsymbol{Q}_h, \boldsymbol{A})_{\mathcal{T}_h}\,, \\
b(\delta\boldsymbol{u}_h, \boldsymbol{A}) &= -\left(\delta\boldsymbol{u}_h, \nabla\cdot\boldsymbol{A}\right)_{\mathcal{T}_h}\,, \\
c(\delta\hat{\boldsymbol{u}}_h, \boldsymbol{A}) &= \langle\delta\hat{\boldsymbol{u}}_h, \boldsymbol{A}\cdot\boldsymbol{n}\rangle_{\partial\mathcal{T}_h}\,, \\
n(\boldsymbol{A}) &= -\left(\boldsymbol{Q}_h, \boldsymbol{A}\right)_{\mathcal{T}_h} + \left(\boldsymbol{u}_h, \nabla\cdot\boldsymbol{A}\right)_{\mathcal{T}_h} - \langle\hat{\boldsymbol{u}}_h, \boldsymbol{A}\cdot\boldsymbol{n}\rangle_{\partial\mathcal{T}_h}\,, \\
h(\delta\boldsymbol{Q}_h, \boldsymbol{a}) &= \left(\frac{\partial\boldsymbol{F}}{\partial\boldsymbol{Q}}\delta\boldsymbol{Q}_h, \nabla\boldsymbol{a}\right)_{\mathcal{T}_h} - \left\langle\frac{\partial\hat{\boldsymbol{F}}}{\partial\boldsymbol{Q}}\delta\boldsymbol{Q}_h\cdot\boldsymbol{n}, \boldsymbol{a}\right\rangle_{\partial\mathcal{T}_h}\,, \\
d(\delta\boldsymbol{u}_h, \boldsymbol{a}) &= \left(\frac{\partial\boldsymbol{F}}{\partial\boldsymbol{u}}\delta\boldsymbol{u}_h, \nabla\boldsymbol{a}\right)_{\mathcal{T}_h} - \left\langle\frac{\partial\hat{\boldsymbol{F}}}{\partial\boldsymbol{u}}\delta\boldsymbol{u}_h\cdot\boldsymbol{n}, \boldsymbol{a}\right\rangle_{\partial\mathcal{T}_h} + \left(\frac{\partial\boldsymbol{s}}{\partial\boldsymbol{u}}\delta\boldsymbol{u}_h, \boldsymbol{a}\right)_{\mathcal{T}_h}\,, \\
e(\delta\hat{\boldsymbol{u}}_h, \boldsymbol{a}) &= -\left\langle\frac{\partial\hat{\boldsymbol{F}}}{\partial\hat{\boldsymbol{u}}}\delta\hat{\boldsymbol{u}}_h\cdot\boldsymbol{n}, \boldsymbol{a}\right\rangle_{\partial\mathcal{T}_h}\,, \\
f(\boldsymbol{a}) &= -\left(\boldsymbol{F}_h, \nabla\boldsymbol{a}\right)_{\mathcal{T}_h} + \left\langle\hat{\boldsymbol{F}}_h\cdot\boldsymbol{n}, \boldsymbol{a}\right\rangle_{\partial\mathcal{T}_h} - \left(\boldsymbol{s}, \boldsymbol{a}\right)_{\mathcal{T}_h}\,, \\
k(\delta\boldsymbol{Q}_h, \boldsymbol{\mu}) &= \left\langle\frac{\partial\hat{\boldsymbol{F}}}{\partial\boldsymbol{Q}}\delta\boldsymbol{Q}_h\cdot\boldsymbol{n}, \boldsymbol{\mu}\right\rangle_{\partial\mathcal{T}_h} - \left\langle\frac{\partial\boldsymbol{g}_N}{\partial\boldsymbol{Q}}\delta\boldsymbol{Q}_h, \boldsymbol{\mu}\right\rangle_{\partial\Omega_N}\,, \\
l(\delta\boldsymbol{u}_h, \boldsymbol{\mu}) &= \left\langle\frac{\partial\hat{\boldsymbol{F}}}{\partial\boldsymbol{u}}\delta\boldsymbol{u}_h\cdot\boldsymbol{n}, \boldsymbol{\mu}\right\rangle_{\partial\mathcal{T}_h} - \left\langle\frac{\partial\boldsymbol{g}_N}{\partial\boldsymbol{u}}\delta\boldsymbol{u}_h, \boldsymbol{\mu}\right\rangle_{\partial\Omega_N}\,, \\
m(\delta\hat{\boldsymbol{u}}_h, \boldsymbol{\mu}) &= \left\langle\frac{\partial\hat{\boldsymbol{F}}}{\partial\hat{\boldsymbol{u}}}\delta\hat{\boldsymbol{u}}_h\cdot\boldsymbol{n}, \boldsymbol{\mu}\right\rangle_{\partial\mathcal{T}_h}\,, \\
g(\boldsymbol{\mu}) &= -\left\langle\hat{\boldsymbol{F}}_h\cdot\boldsymbol{n}, \boldsymbol{\mu}\right\rangle_{\partial\mathcal{T}_h} + \langle\boldsymbol{g}_N, \boldsymbol{\mu}\rangle_{\partial\Omega_N}\,.
\end{aligned}
\tag{3.24}
$$

Note that the superscript $n$ denoting the current iteration has been omitted above to simplify notation. Derivatives with respect to solution variables $\boldsymbol{Q}$, $\boldsymbol{u}$, and $\hat{\boldsymbol{u}}$ are analytically derived functions based on definitions in equation (3.14). Appendix B provides details of these sensitivity functions.

## 3.3 Boundary Conditions

The system defined by equations (3.21), (3.22), and (3.23) can be solved to find a solution which satisfies the governing equations, however, the choice of boundary conditions determines how closely the solution captures the behavior of a physical EHD thruster. The two primary governing equations, Gauss's Law and conservation

of charge, each require one boundary condition for every surface in the domain $\Omega$. An insufficient number of boundary conditions may result in a non-unique solution while over-constraining the system may prevent the solution from converging due to incompatibilities. This section describes the boundary condition options that are available and strategies for applying conditions to allow for convergent numerical solutions that adequately reflect physical reality.

### 3.3.1 Dirichlet Boundary Conditions

Dirichlet boundary conditions are also known as essential boundary conditions. They are essential in that at least one surface in the domain must have a Dirichlet boundary condition specified. Failure to satisfy this requirement leads to a non-unique solution since a scalar solution plus a constant also satisfies the governing system of equations. This is particularly true for Gauss's Law but a Neumann charge injection boundary condition may be sufficient for the conservation of charge equation in the system.

For any EHD thruster geometry, the potential at the emitter and collector electrodes are prescribed since these parameters are set directly on the thruster power supply. An EHD thruster is meant to be operated in an open environment where the potential is zero an infinite distance away from the thruster device. Such a boundary condition cannot be directly implemented in a numerical model due to computational limitations. Instead, schemes such as the ballooned boundary method [46, 47] or exterior to interior mapping [34] are used to account for the conditions at infinity on the truncated domain in CG-FEM problems. Further development of HDG methods is required to find a scheme which will achieve the same goal. In the present work Dirichlet conditions on the truncated boundary are left unspecified. The default condition in this case is the natural boundary condition as described in section 3.3.2.

The charge density on the emitter electrode surface may also be specified as a Dirichlet boundary condition. The distribution of charge on the surface is not known a priori but may be calculated iteratively to satisfy a given requirement. The charge injection conditions described in section 3.3.2 are examples of requirements which can

be used to arrive at an appropriate distribution of charge. In cases where the size of the emitter is small relative to the domain and there is sufficient symmetry, assuming a constant charge density on the emitter surface may be a reasonable approximation [10].

### 3.3.2 Neumann Boundary Conditions

Neumann boundary conditions are requirements imposed on normal fluxes in the HDG formulation. In the present problem, the fluxes are the electric field and the current density. These fluxes are typically not known a priori and typically vary along boundaries. It is necessary to specify an outflow condition otherwise the natural boundary condition applies. The HDG formulation requires integration of the numerical flux through all surfaces in the domain which is in effect requiring

$$\hat{\boldsymbol{F}} \cdot \boldsymbol{n} = \boldsymbol{g}_N = 0 \text{ on } \partial\Omega_N, \tag{3.25}$$

if $\boldsymbol{g}_N$ is not otherwise specified. This constitutes the natural boundary condition and applies on the the truncated domain boundary. This condition would positively impact the calculated performance of an EHD thruster by forcing all emitted current to be collected at the anode. An outflow condition is set by specifying

$$\hat{\boldsymbol{F}} \cdot \boldsymbol{n} = \boldsymbol{g}_N = \boldsymbol{F} \cdot \boldsymbol{n} \text{ on } \partial\Omega_N. \tag{3.26}$$

This overrides the natural condition and allows any value of flux on the boundary since, for a converged solution where $\hat{\boldsymbol{u}} = \boldsymbol{u}|_{\partial K}$,

$$\hat{\boldsymbol{F}} \cdot \boldsymbol{n} - \boldsymbol{F} \cdot \boldsymbol{n} = -\tau(\boldsymbol{u} - \hat{\boldsymbol{u}}) = 0 \text{ on } \partial\Omega_N. \tag{3.27}$$

The outflow condition for current density should be applied to any collector electrodes.

### Charge Injection

The charge injection boundary condition applied to the emitter electrode is an approximation of the impact ionization occurring in the high field region surrounding the emitter. Cagnoni et al. provide a summary of various charge injection models for an emitter electrode [4]. The first model applies a uniform current density to the emitter surface and is expressed by

$$\hat{\boldsymbol{F}}_2 \cdot \boldsymbol{n} = \boldsymbol{g}_N = -\frac{I_m}{A_e} \text{ on } \partial\Omega_N, \tag{3.28}$$

where $\hat{\boldsymbol{F}}_2$ refers to the boundary flux associated with the conservation of charge equation, $I_m$ is a prescribed total current, and $A_e$ is the surface area of the emitter. $I_m$ can be an experimentally measured current. This model does not allow predictive simulations since the total current is a prescribed value and will not accurately represent the current density distribution around electrodes of complex geometry.

The next model relies on correlations such as Peek's law to set a corona onset field, $E_{on}$, and enforces Kaptsov's hypothesis in a pointwise manner on the emitter surface. The model can be expressed as a Neumann condition on the current flux by

$$\hat{\boldsymbol{F}}_2 \cdot \boldsymbol{n} = \boldsymbol{g}_N = -\rho\mu E_{on} \text{ on } \partial\Omega_N, \tag{3.29}$$

where $\rho$ is the charge density solution at the current iterate. While this boundary condition can be implemented directly in the HDG formulation, the solution will be non-unique since the trivial solution for charge density automatically satisfies (3.29). The boundary condition must be enforced in a manner similar to the approach used for the FEM/MOC scheme in section 2.1 or with augmented residual equations as demonstrated by Feng [14]. The FEM/MOC approach updates the distribution of charge density on the emitter surface in an outer loop until the converged HDG solution satisfies (3.29) on $\partial\Omega_N$.

The charge injection model (3.29) allows for abrupt changes in the charge density which are difficult for polynomial basis functions to accurately represent. Cagnoni

et al. found that (3.29) would introduce numerical oscillations if not treated with sufficient under-relaxation [4]. They proposed a smoother but less accurate form of (3.29) which can be expressed as

$$\hat{\boldsymbol{F}}_2 \cdot \boldsymbol{n} = \boldsymbol{g}_N = \boldsymbol{F}_2 \cdot \boldsymbol{n} + \rho\mu E_{on} - \rho_{ref}\mu E_{on} \exp\left(\frac{-\vec{E} \cdot \boldsymbol{n} - E_{on}}{E_{ref}}\right) \text{ on } \partial\Omega_N. \quad (3.30)$$

In this case, the trivial solution for $\rho$ does not automatically satisfy the boundary condition. The choice of the reference values, $\rho_{ref}$ and $E_{ref}$, determines how sharply the current flux increases with $\vec{E} \cdot \boldsymbol{n}$. The normal electric field is set with a negative sign in (3.30) to account for the sense of the normal vector, which is always an outward normal.

## 3.4 Implementation

The HDG formulation is implemented using MATLAB R2013a. The solver is constructed to be independent of problem geometry, boundary conditions, and mesh. Information specific to a particular problem is contained in an application structure. This information includes boundary condition functions, problem constants, convergence criteria, and problem geometry. Mesh data and master element data are independent of boundary conditions but construction of the mesh requires geometry information from the application structure. Mesh constructors also require the order of polynomial basis functions. The value of the polynomial basis functions and their derivatives at Gauss points are contained in the master element data structure. The master element data structure also contains the location of element interior nodes which support the polynomial basis functions in barycentric coordinates.

### 3.4.1 Meshing

The triangulation on the domain is calculated using the *adaptmesh* command from the PDE Toolbox add-in for MATLAB. This function uses the MATLAB Delaunay triangulation routine to create the initial triangulation and then refines the mesh

based on the accuracy of the mesh in solving the Laplace equation with first order basis functions. The maximum number of triangles can be specified as an input to the function. Other meshing tools may also be used such as the DistMesh suite of tools made available by Per-Olaf Persson [44]. DistMesh relies on distance functions and truss force balance simulations to ensure smooth element size variation and ideal element shapes. This proved problematic for meshing some of the geometries investigated here because of the size difference between the emitter electrodes and the rest of the domain. The DistMesh force balance simulations had difficulty converging in the vicinity of the small emitter electrode. The present implementation only takes advantage of the distance function tools in the DistMesh package for locating element face nodes on curved boundaries.

Once the triangulation is complete and triangle to node connectivity data is available, element face to triangle connectivity is determined. Element faces are constructed such that the vector described by the start and end points of a face is directed in the counter-clockwise sense along the element boundary. Faces which are on a domain boundary are identified and associated with a boundary number. This facilitates application of boundary conditions. Triangles which share a given face are also identified.

The mesh constructor also defines a distance function for the domain which calculates the distance of a given point to the closest domain boundary. The distance function is stored in the mesh structure. The element interior node coordinates are in general calculated using the element vertex coordinates and the barycentric coordinates of the nodes on the master element. Nodes which are intended to lie on a curved boundary must be moved towards the boundary until the distance function for those points is zero. Figure 3-1 shows an example of a fifth order DG element and associated nodes on a curved boundary.

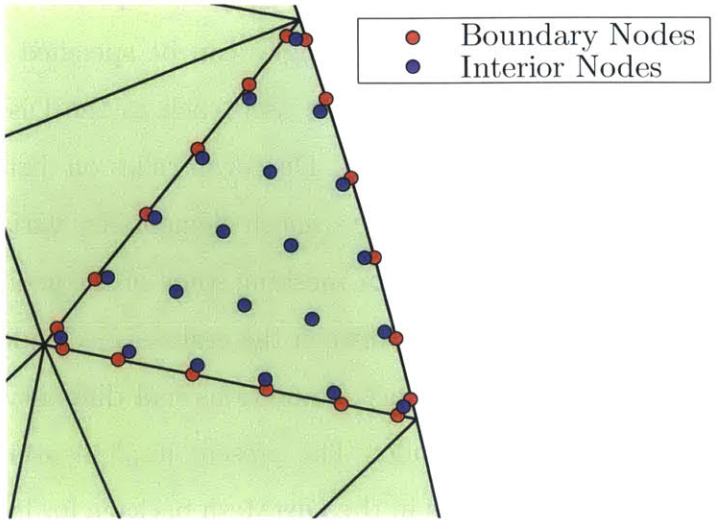


Figure 3-1: Fifth order DG element, nodes are shown with small perturbations to avoid overlaps.

### 3.4.2 Solving

Equations (3.21) and (3.22) must be satisfied on each element as well as the entire domain. The linearized system of equations results in a matrix system

$$\begin{bmatrix} \mathbb{A}_K & \mathbb{B}_K & \mathbb{C}_K \\ \mathbb{H}_K & \mathbb{D}_K & \mathbb{E}_K \\ \mathbb{K}_K & \mathbb{L}_K & \mathbb{M}_K \end{bmatrix} \begin{bmatrix} \partial \mathbb{Q}_K \\ \partial \mathbb{U}_K \\ \partial \hat{\mathbb{U}}_K \end{bmatrix} = \begin{bmatrix} \mathbb{N}_K \\ \mathbb{F}_K \\ \mathbb{G}_K \end{bmatrix} \tag{3.31}$$

where $\partial \mathbb{Q}_K$, $\partial \mathbb{U}_K$, and $\partial \hat{\mathbb{U}}_K$ correspond to the vectors of the solution degrees of freedom on a given element. Since the solution is allowed to be discontinuous between elements, the solution on element interior degrees of freedom is equal to

$$\begin{bmatrix} \partial \mathbb{Q}_K \\ \partial \mathbb{U}_K \end{bmatrix} = \begin{bmatrix} \mathbb{A}_K & \mathbb{B}_K \\ \mathbb{H}_K & \mathbb{D}_K \end{bmatrix}^{-1} \begin{bmatrix} \mathbb{N}_K \\ \mathbb{F}_K \end{bmatrix} - \begin{bmatrix} \mathbb{A}_K & \mathbb{B}_K \\ \mathbb{H}_K & \mathbb{D}_K \end{bmatrix}^{-1} \begin{bmatrix} \mathbb{C}_K \\ \mathbb{E}_K \end{bmatrix} \partial \hat{\mathbb{U}}_K. \tag{3.32}$$

The matrix composed of $\mathbb{A}_K$, $\mathbb{B}_K$, $\mathbb{H}_K$, and $\mathbb{D}_K$ is block diagonal and invertible. The remaining matrix equation is

$$\begin{bmatrix} \mathbb{K}_K & \mathbb{L}_K \end{bmatrix} \begin{bmatrix} \partial \mathbb{Q}_K \\ \partial \mathbb{U}_K \end{bmatrix} + \mathbb{M}_K \partial \hat{\mathbb{U}}_K = \mathbb{G}_K. \tag{3.33}$$

Substituting (3.32) into (3.33) yields

$$\underbrace{\mathbb{M}_K - \begin{bmatrix} \mathbb{K}_K & \mathbb{L}_K \end{bmatrix} \begin{bmatrix} \mathbb{A}_K & \mathbb{B}_K \\ \mathbb{H}_K & \mathbb{D}_K \end{bmatrix}^{-1} \begin{bmatrix} \mathbb{C}_K \\ \mathbb{E}_K \end{bmatrix}}_{\mathbb{J}_K} \partial \hat{\mathbb{U}}_K = \underbrace{\mathbb{G}_K - \begin{bmatrix} \mathbb{K}_K & \mathbb{L}_K \end{bmatrix} \begin{bmatrix} \mathbb{A}_K & \mathbb{B}_K \\ \mathbb{H}_K & \mathbb{D}_K \end{bmatrix}^{-1} \begin{bmatrix} \mathbb{N}_K \\ \mathbb{F}_K \end{bmatrix}}_{\mathbb{R}_K}, \tag{3.34}$$

where $\mathbb{J}_K$ is the element Jacobian matrix for scalar solution degrees of freedom on the element boundary and $\mathbb{R}_K$ is the corresponding residual vector. $\mathbb{J}_K$ and $\mathbb{R}_K$ can then be stamped into the global Jacobian matrix $\mathbb{J}$ and residual vector $\mathbb{R}$. The final matrix system for the scalar solution on element face degrees of freedom is

$$\mathbb{J} \partial \hat{\mathbb{U}} = \mathbb{R}. \tag{3.35}$$

The system can be reduced further for matrix inversion by temporarily eliminating rows and columns in $\mathbb{J}_K$, $\partial \hat{\mathbb{U}}$, and $\mathbb{R}$ associated with boundaries where Dirichlet conditions apply. Once $\partial \hat{\mathbb{U}}$ is calculated using built-in MATLAB functions to invert the system, the interior solution is retrieved on an element-by-element basis using (3.32). Matrix assembly and solution retrieval are suitable for parallel processing implementation since only current solution information for a given element is required to either construct the element Jacobian matrix or the element interior solution.

### 3.4.3 Post-Processing

Thruster performance parameters must be post-processed from the raw solution. The thrust component in the direction of a unit vector $\boldsymbol{c}$ is calculated by

$$T = \left(\rho_h \vec{E}_h, \boldsymbol{c}\right)_{\mathcal{T}_h}. \tag{3.36}$$

The total current is found by integrating the current density on the surface of any emitting electrode

$$I = \left\langle \mu \rho_h \vec{E}_h \cdot \boldsymbol{n}, l \right\rangle_{\partial\Omega_{emit}}, \tag{3.37}$$

where $l$ is the length of the emitting electrode.

## 3.5 Validation Procedure

The HDG implementation will be validated with the following approach:

1. Use the model problem to assess convergence rate.
2. Assess the charge injection boundary condition by offsetting the inner cylinder in the model problem.
3. Simulate single stage and dual stage EHD thrusters based on geometry tested by Masuyama and Barrett [29, 30].

The model problem inner cylinder radius is set to $r_a = 0.01\,\text{m}$. An outer cylinder radius of $r_b = 0.4527\,\text{m}$ corresponds to $\rho_0 = 10^{-5}\,\text{Cm}^{-3}$ and $\phi_0 = 5000\,\text{V}$ in equation (2.13). The system is also assumed to be at atmospheric pressure (76 cmHg) and 20 °C. Figure 3-2 shows the resulting analytical solution for $\phi$ and $\rho$ from equations (2.11a) and (2.12). The gradient of $\rho$ close to the emitter is very large and may pose problems for convergence if the mesh density near the emitter is not sufficient. Another approach to handling the large gradient is to successively ramp $\rho$ at the emitter surface until the target value $\rho_0$ is reached. The converged solution for a given $\rho$ at the emitter surface is used as the initial solution for the subsequent case.

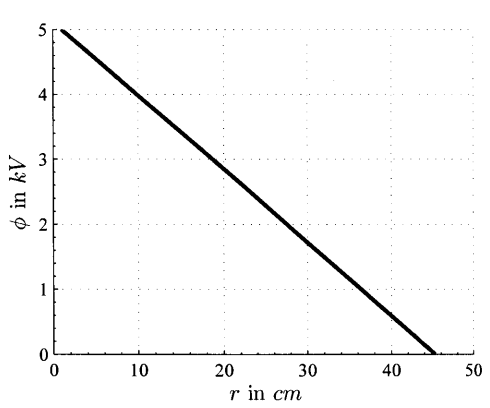


(a) Potential Solution

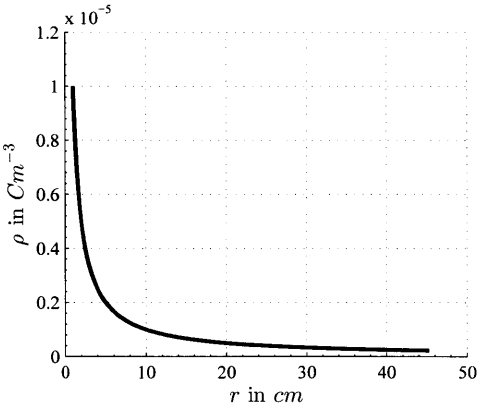


(b) Charge Density Solution

Figure 3-2: Model problem solution for $r_a = 0.01\,\text{m}$, $\rho_0 = 10^{-5}\,\text{Cm}^{-3}$, and $\phi_0 = 5\,\text{kV}$.

The convergence rate, $r$, for scalar unknowns is assessed in the $L^2$ norm using

$$\lim_{n\to\infty} \frac{\|u_h^{n+1} - u\|}{\|u_h^n - u\|^r} = C, \tag{3.38}$$

where $C > 0$ is a finite constant, $u_h^n$ is the approximate solution at iteration $n$, and $u$ is the true solution [20]. The solution error is generally expressed as $e^n = u_h^n - u$. Equation (3.38) is reformulated to simplify determination of the convergence rate by expressing it as

$$\log(\|e^{n+1}\|) = r\log(\|e^n\|) + \log(C). \tag{3.39}$$

The convergence rate $r$ is then simply the slope of the best fit line for a plot of $\log(\|e^{n+1}\|)$ vs. $\log(\|e^n\|)$.

The charge injection boundary condition per equation (3.30) requires a relationship between $\rho_{ref}$ and $E_{ref}$. This is obtained for a given applied voltage by ramping $\rho$ at the emitter surface and finding the corresponding converged solutions. Per equation (1.3) (Peek's law) with $\delta \approx 1.02$, $m_s = 1$, $c = .308$, $r = r_a$, and $E_0 = 31\,^{\text{kV}}/_{\text{cm}}$, the critical field strength is $E_{on} = E_{crit} \approx 41.13\,^{\text{kV}}/_{\text{cm}}$. Using the model problem settings described previously, $E_r$ from equation (2.11b) is approximately $0.11\,^{\text{kV}}/_{\text{cm}}$. The fact that $E_{on} \gg E_r$ indicates that the analytical solution is not consistent with the corona discharge physics; either the applied voltage is too low or the charge density at the emitter is too high.

The single stage thruster geometry tested by Masuyama & Barrett [29, 30] consisted of a 32 AWG (0.202 mm diameter) tinned copper wire emitter electrode and a 0.635 cm diameter 6061 aluminum tube collector electrode (see figure 1-1). Both electrodes were 40 cm long. The $d = 1$ cm electrode spacing is investigated here first using the experimentally determined current-voltage characteristic in the homogeneous boundary condition equation (3.28) and then using the smoothed charge injection model given by equation (3.30). In this case the parallel wire coefficients from table 1.1 are more appropriate for equation (1.3); the critical electric field strength is $E_{on} \approx 121.1\,{}^{\mathrm{kV}}/_{\mathrm{cm}}$.

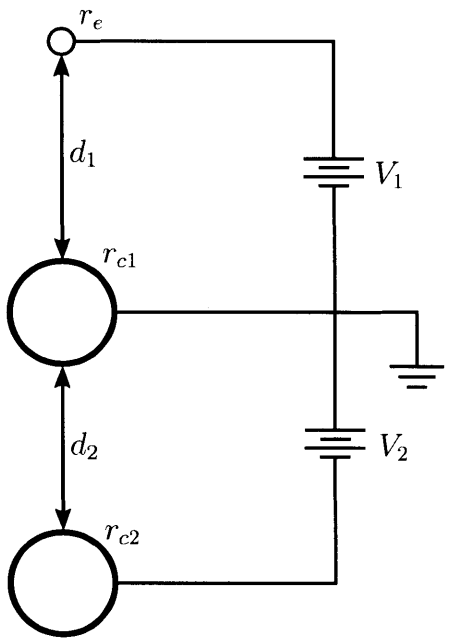


Figure 3-3: Dual stage thruster geometry.

Figure 3-3 illustrates the dual stage thruster geometry tested by Masuyama & Barrett [29, 30]. The intermediate electrode is a single strand 4 AWG (5.189 mm diameter) solid copper wire. The emitter electrode and collector electrode are the same as the single stage case. The electrode spacings $d_1 = 1$ cm and $d_2 = 3$ cm are investigated in the present work. The applied voltage $V_2$ is maintained at 20 kV while $V_1$ is varied.

# Chapter 4

# Results

Numerical results from the validation procedure described in the previous chapter are presented here. The model problem investigation involves three phases: performance against analytical solution, determination of charge injection reference parameters, and evaluation of charge injection boundary condition. The results of the model problem inform the charge injection boundary condition configuration in subsequent sections. A single stage thruster numerical model is used to evaluate the predictive capability of the HDG implementation. Finally, a dual stage thruster numerical model is used to evaluate the HDG implementation for more complex geometries. Analysis meshes are shown in Appendix D and are generally composed of less than 4000 elements to facilitate solving on a personal computer. Each matrix assembly and inversion iteration takes less than one minute on a personal computer running Windows 7 with 4 processing cores and 8 Gb of RAM. A high resolution mesh of 11428 elements is used for part of the single stage thruster modeling and requires a desktop computer with 16 Gb of RAM and 6 processing cores to solve.

## 4.1 Model Problem

The model problem geometry consists of concentric cylinders for comparison against the analytical solution. The investigation for determining and testing the charge injection parameters requires offsetting the emitter electrode. The outer cylinder is

maintained at zero potential while the potential applied to the emitting electrode is varied.

### 4.1.1 Approximation of Analytical Solution

As mentioned in section 3.5, the high gradients near the emitter electrode necessitate ramping the charge density at the emitter over the course of four analysis cases. The charge density Dirichlet boundary condition for each case is expressed as a factor multiplying $\rho_0$ which is the emitter charge density corresponding to the analytical solution.

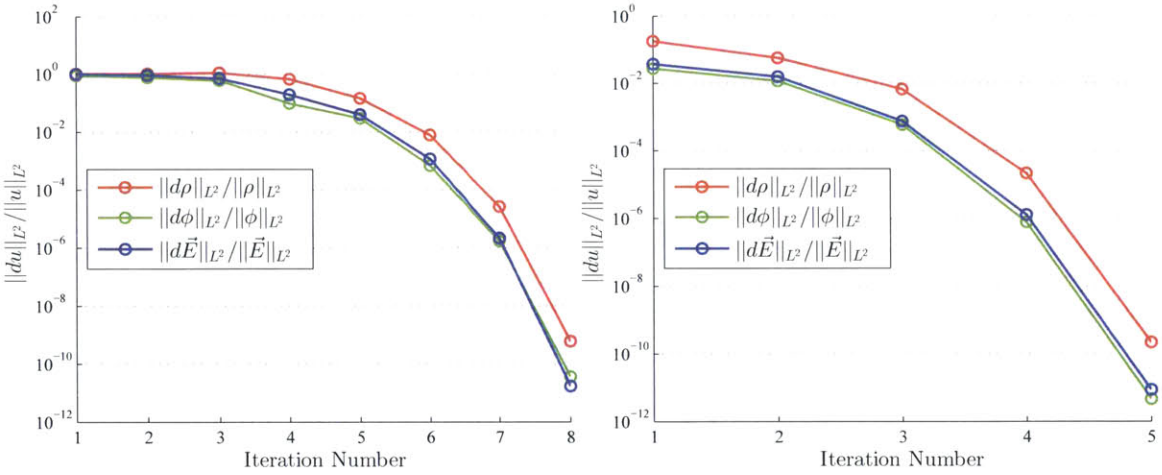


(a) Normalized residuals for $0.2 \times \rho_0$ case. (b) Normalized residuals for $1.0 \times \rho_0$ case.

Figure 4-1: Model problem normalized residuals for $r_a = 0.01\,\text{m}$, $\rho_0 = 10^{-5}\,\text{Cm}^{-3}$, and $\phi_0 = 5\,\text{kV}$.

Figure 4-1 shows the normalized residuals for the first and last cases. The first case requires more iterations to arrive at a converged solution since the initial solution is the solution to the Laplace equation where charge density is zero everywhere. The initial solution for the last case includes the charge density from the previous case which is a closer approximation to the analytical solution. Attempting to solve the final case without the intermediate solutions results in instabilities in the charge density solution near the emitter. Non-physical negative values of charge density appear which cause the solution to diverge.

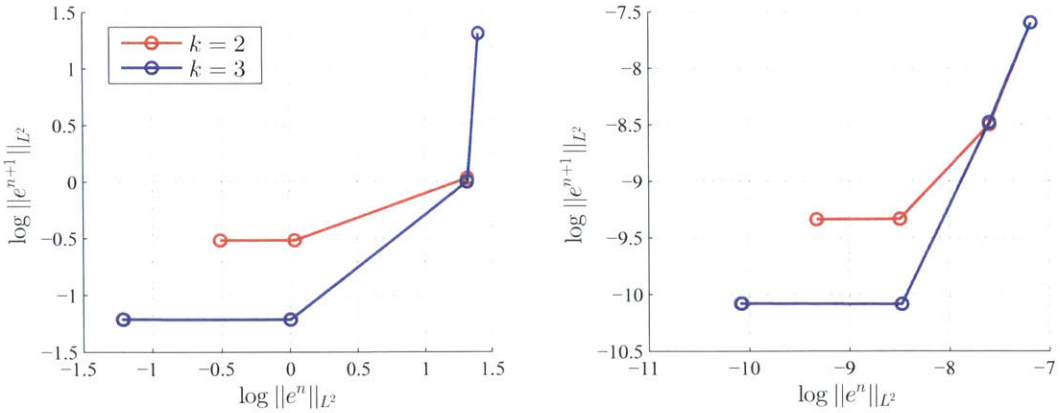


(a) Error schedule for potential.

(b) Error schedule for charge density.

Figure 4-2: Plot of $\log\|e^{n+1}\|_{L^2}$ vs. $\log\|e^n\|_{L^2}$ for identical meshes with basis functions of order $k$.

The error schedules are shown in figure 4-2 and table 4.1. The error is reduced with an increase in order of the polynomial basis. The convergence rate for $\phi$ is large until the solution approaches the analytical solution. The convergence rate for $\rho$ is initially quadratic but reduces as the analytical solution is approached. The $k = 3$ case indicates that the quadratic convergence rate can be maintained for more iterations with higher order basis functions.

Table 4.1: Error schedules for $\phi$ and $\rho$ showing convergence rate for each iteration, polynomial order $k = 2$.

(a) Error schedule for $\phi$

| $n$ | $\log\|e^n\|_{L^2}$ | $\log\|e^{n+1}\|_{L^2}$ | $r$ |
|---|---|---|---|
| 0 | 1.40 | 1.31 | - |
| 1 | 1.31 | .034 | 14.6 |
| 2 | .034 | −.51 | .43 |
| 3 | −.51 | −.51 | $-5.1 \times 10^{-4}$ |
| 4 | −.51 | −.51 | $-6.0 \times 10^{-6}$ |

(b) Error schedule for $\rho$

| $n$ | $\log\|e^n\|_{L^2}$ | $\log\|e^{n+1}\|_{L^2}$ | $r$ |
|---|---|---|---|
| 0 | −7.18 | −7.60 | - |
| 1 | −7.60 | −8.50 | 2.2 |
| 2 | −8.50 | −9.33 | .93 |
| 3 | −9.33 | −9.33 | $2.7 \times 10^{-3}$ |
| 4 | −9.33 | −9.33 | $5.5 \times 10^{-6}$ |

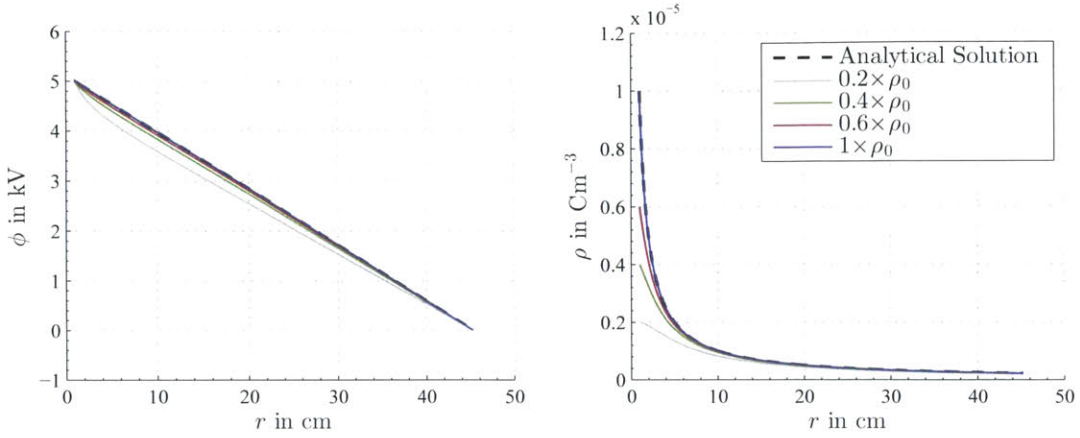


(a) Potential solution. (b) Charge density solution.

Figure 4-3: Model problem solution for $r_a = 0.01\,\mathrm{m}$, $\rho_0 = 10^{-5}\,\mathrm{Cm}^{-3}$, and $\phi_0 = 5\,\mathrm{kV}$.

Figure 4-3 shows the potential and charge density solutions as a function of radial distance from the inner emitter electrode to the outer cylinder for each case. The final approximate solution is a close match to the analytical solution. The potential solution for the first case and the last case are within 9% of the analytical solution. The charge density solution for the first and last case on the other hand diverges at $r < 5\,\mathrm{cm}$. This underscores the importance of including intermediate solutions to ensure convergence for the charge density. The maximum error normalized by applied potential and charge is at most on the order of $10^{-3}$ per figure 4-4.

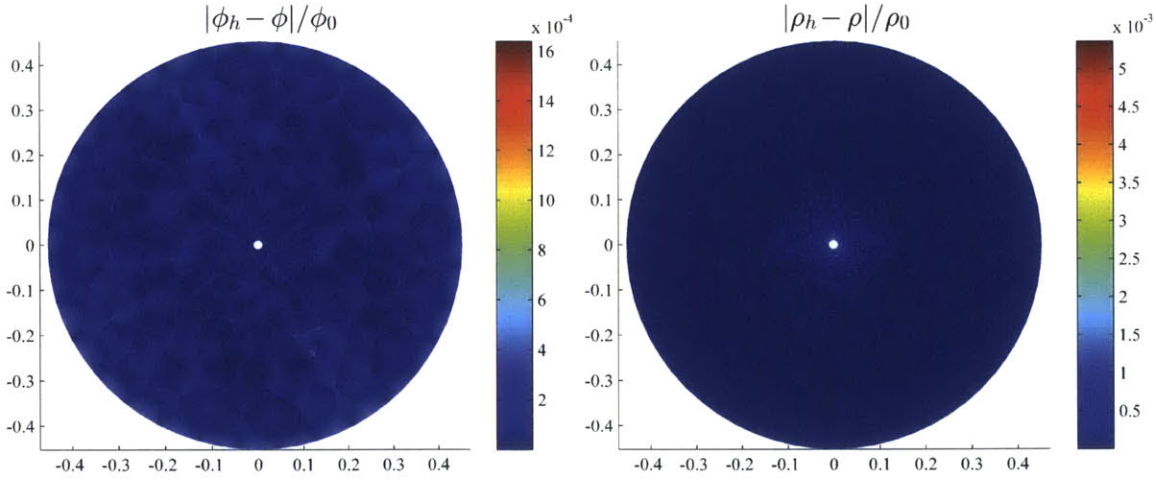


(a) Potential normalized error. (b) Charge density normalized error.

Figure 4-4: Scalar solution errors for $r_a = 0.01\,\mathrm{m}$, $\rho_0 = 10^{-5}\,\mathrm{Cm}^{-3}$, and $\phi_0 = 5\,\mathrm{kV}$.

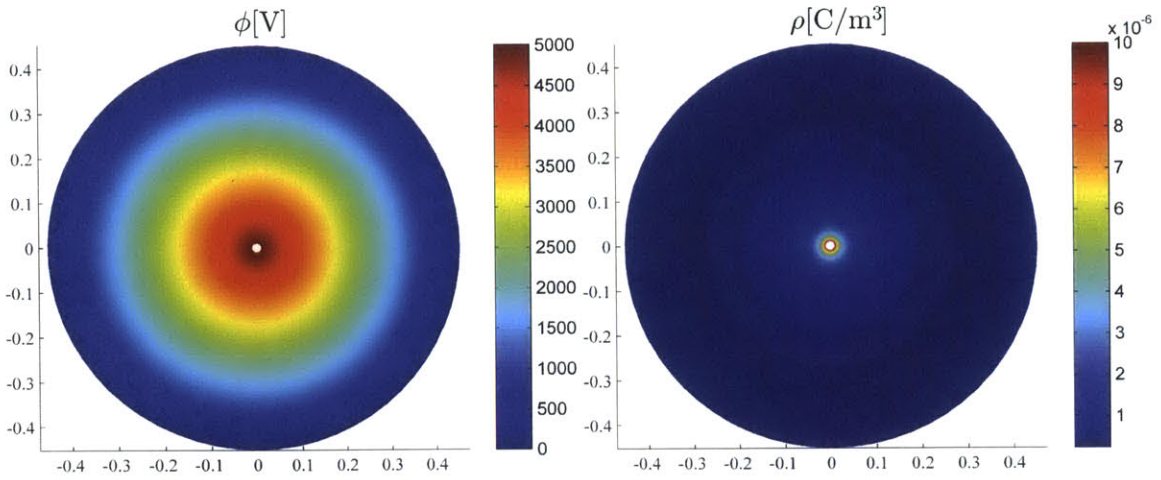


(a) Potential solution.

(b) Charge density solution.

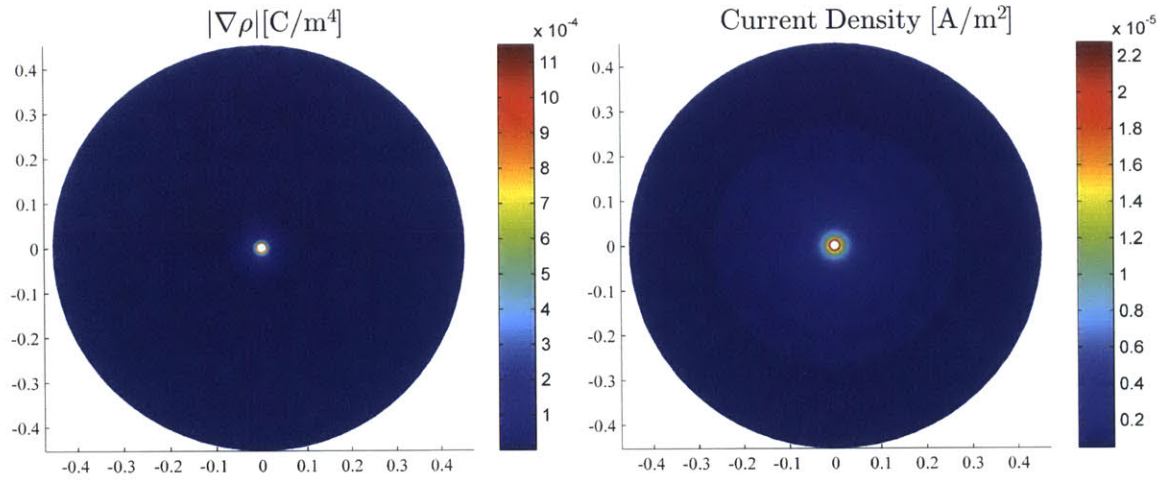


(c) Charge density gradient.

(d) Current density solution.

Figure 4-5: Model problem solution for $r_a = 0.01\,\text{m}$, $\rho_0 = 10^{-5}\,\text{Cm}^{-3}$, and $\phi_0 = 5\,\text{kV}$.

The solution contour plots in figure 4-5 show that the potential, charge density, charge density gradient, and current density vary smoothly over the domain. The discontinuity across element boundaries for the approximate solution is not apparent.

### 4.1.2 Determination of $\rho_{ref}$ and $E_{ref}$

The model problem geometry is modified such that the inner electrode is offset radially by $r_b/2$. Given that the critical field strength is $41.13\,^{\mathrm{kV}}/_{\mathrm{cm}}$ and $E_r = 0.11\,^{\mathrm{kV}}/_{\mathrm{cm}}$, the applied voltage must be increased. Per figure 4-6, a minimum applied voltage of 150 kV ensures the critical field strength is exceeded. Figure 4-7 shows the maximum and minimum electric field at the emitter surface for $\rho_0$ from $2 \times 10^{-7}\,\mathrm{Cm}^{-3}$ to $1 \times 10^{-4}\,\mathrm{Cm}^{-3}$ and applied voltages 150 kV, 200 kV, and 250 kV.

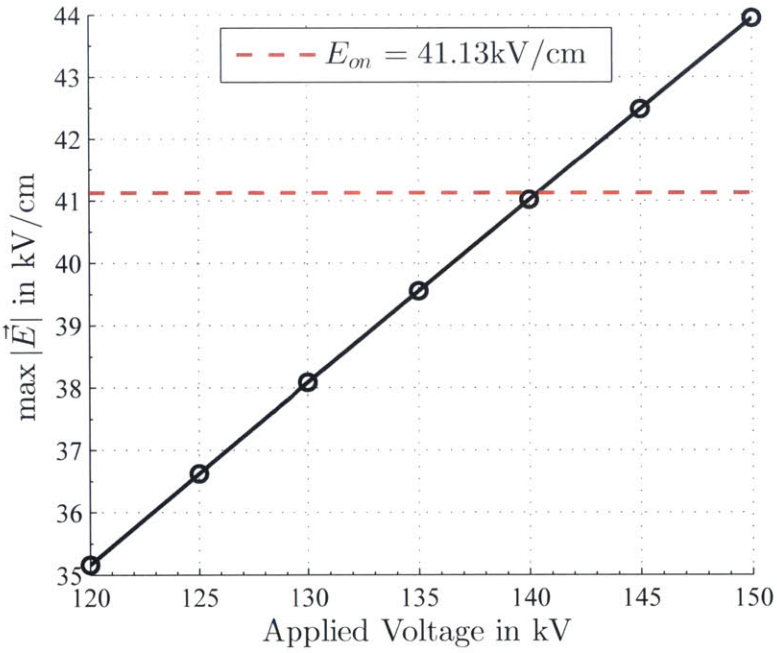


Figure 4-6: Maximum electric field vs. applied voltage for model problem with inner electrode offset by $r_b/2$, $\rho_0 = 0\,\mathrm{Cm}^{-3}$.

Figure 4-6 shows that the maximum electric field increases linearly with applied voltage. This trend is maintained even with $\rho_0 \neq 0$ as shown in figure 4-7. The impact of charge density on the field strength is minimal for $\rho_0 < 1 \times 10^{-6}\,\mathrm{Cm}^{-3}$. For $\rho_0$ changing from $2 \times 10^{-7}\,\mathrm{Cm}^{-3}$ to $1 \times 10^{-7}\,\mathrm{Cm}^{-3}$, the electric field is reduced by 1.7% with an applied electric field of 150 kV. For 250 kV applied voltage, the electric field reduction is 1.1%. This indicates that the change in electric field strength is less sensitive to charge density at higher voltages.

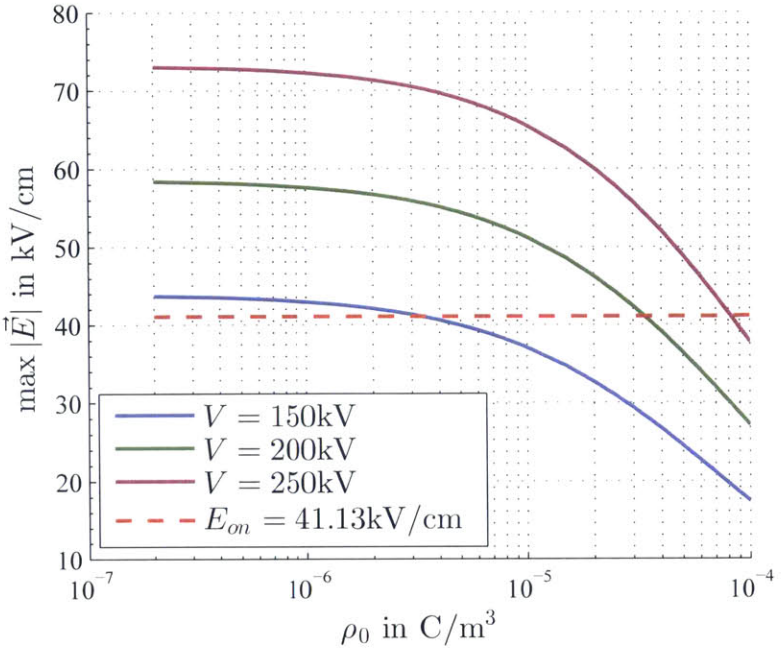


(a) Maximum electric field.

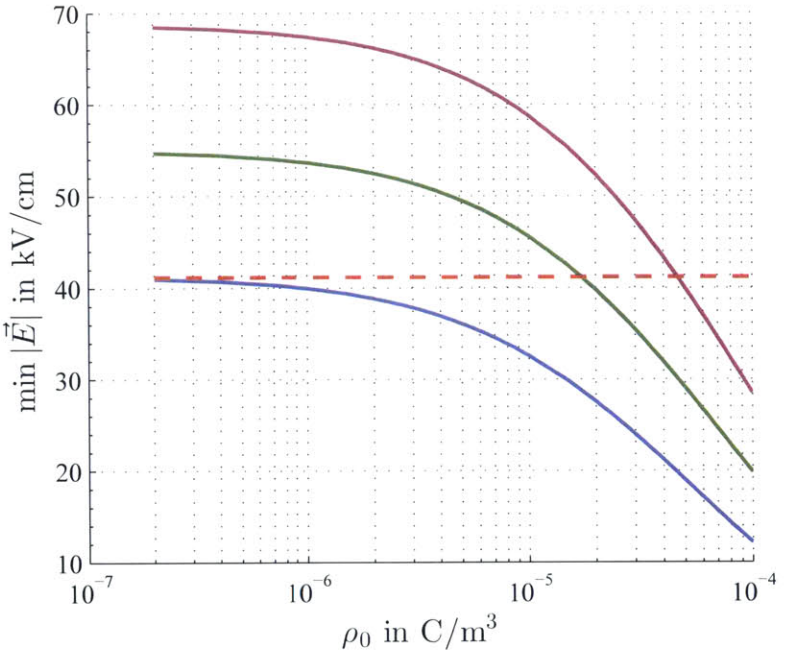


(b) Minimum electric field.

Figure 4-7: Maximum and minimum electric field strength on emitter surface as a function of charge density.

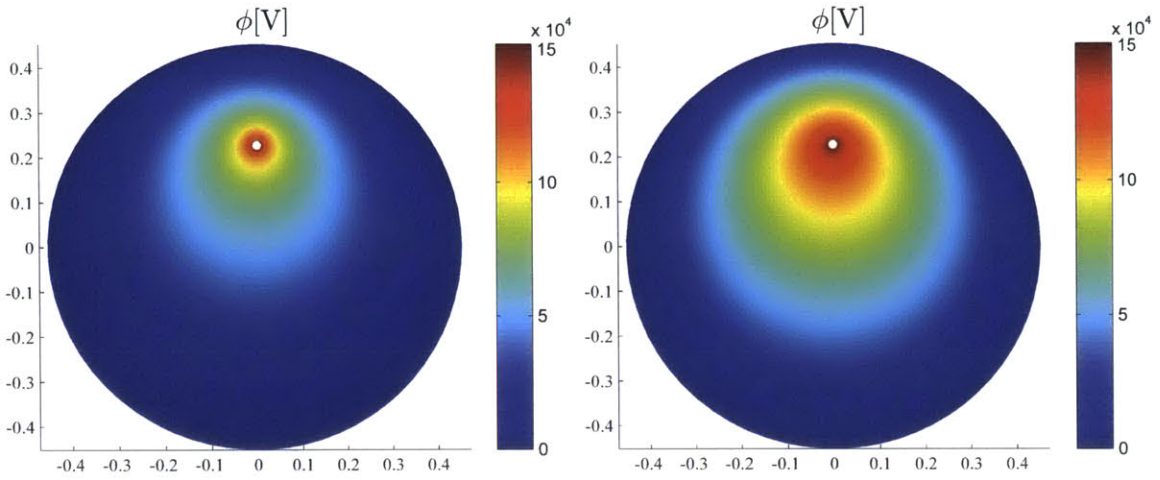


(a) $\rho_0 = 1 \times 10^{-5}\,\mathrm{Cm}^{-3}$. (b) $\rho_0 = 1 \times 10^{-4}\,\mathrm{Cm}^{-3}$.

Figure 4-8: Potential solution for $V = 150\,\mathrm{kV}$.

Figure 4-8 illustrates the impact of increased $\rho_0$ on the electric potential. The increased positive charge raises the potential in vicinity of the emitting electrode. The electric field at the higher charge density is shown in figure 4-9a. The electric field in the small gap between the inner and outer cylinders is elevated compared to the rest of the domain. The charge density distribution as shown in figure 4-9b is no longer uniform and is biased to the region of higher electric field.

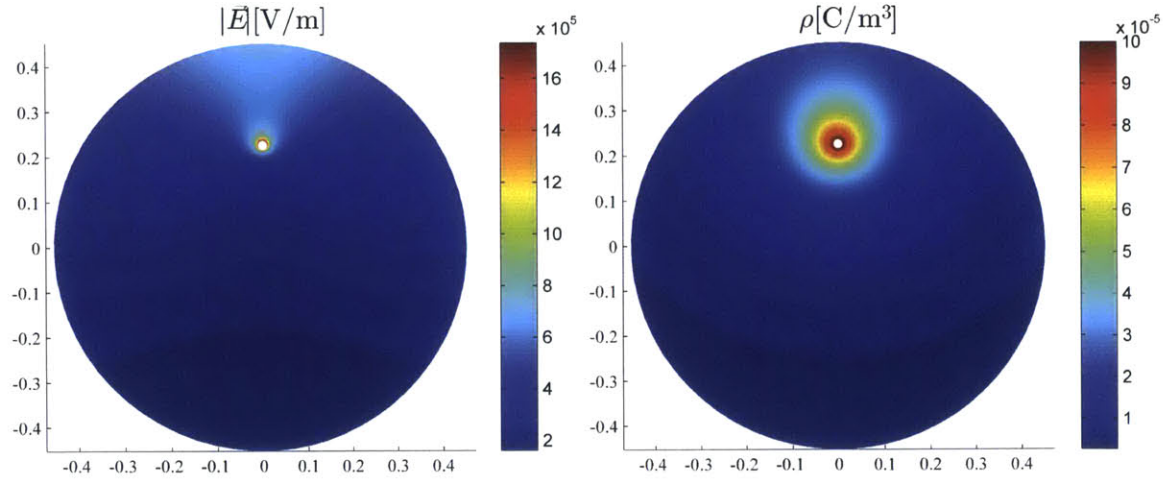


(a) Electric field solution. (b) Charge density.

Figure 4-9: Electric field and charge density solution for $V = 150\,\mathrm{kV}$, $\rho_0 = 1 \times 10^{-4}\,\mathrm{Cm}^{-3}$.

While the current density solution is smooth as shown in figure 4-10b, the charge

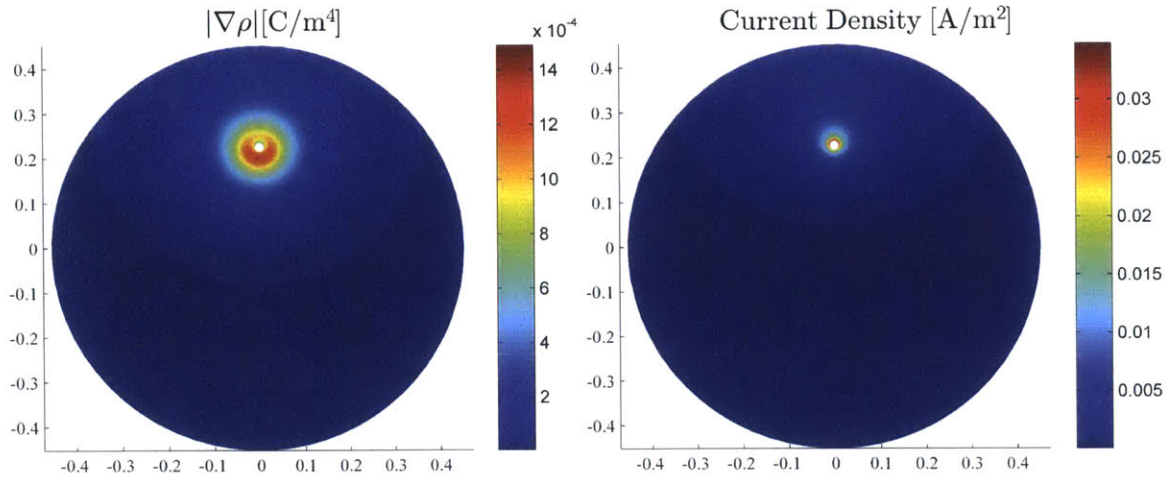


(a) Charge density gradient.

(b) Current density.

Figure 4-10: Charge density gradient and current density solution for $V = 150\,\mathrm{kV}$, $\rho_0 = 1 \times 10^{-4}\,\mathrm{Cm}^{-3}$.

density gradient in figure 4-10a exhibits some faceting. The impact of the discontinuous charge density solution is minimal since the diffusion coefficient $D$ is small in the definition of the current density (see equation (3.5)). The charge density gradient is maximized at the 6 o'clock location on the emitter since the charge density decreases rapidly with distance from the emitter (see figure 4-9b).

The solutions for the axisymmetric case and the offset emitter case have used a uniform charge density applied to the emitter as a Dirichlet boundary condition. The dependence of the electric field at the emitter for various values of $\rho_0$ indicates that there are orders of magnitude for $\rho_0$ where the normal electric field is affected strongly or minimally. Table 4.2 lists the choices for $\rho_{ref}$ and $E_{ref}$ which are investigated in the next section. The range is based on solutions where $V = 150\,\mathrm{kV}$. Case 4 consists of arbitrarily chosen parameters.

Table 4.2: Choices for $\rho_{ref}$ and $E_{ref}$

| Cases | $\rho_{ref}$ $\mathrm{C/m^3}$ | $E_{ref}$ $\mathrm{kV/cm}$ |
|---|---|---|
| 1 | $10^{-4}$ | 12.14 |
| 2 | $10^{-5}$ | 32.58 |
| 3 | $10^{-6}$ | 39.96 |
| 4 | $10^{-6}$ | 1 |

### 4.1.3 Evaluation of Charge Injection Boundary Condition

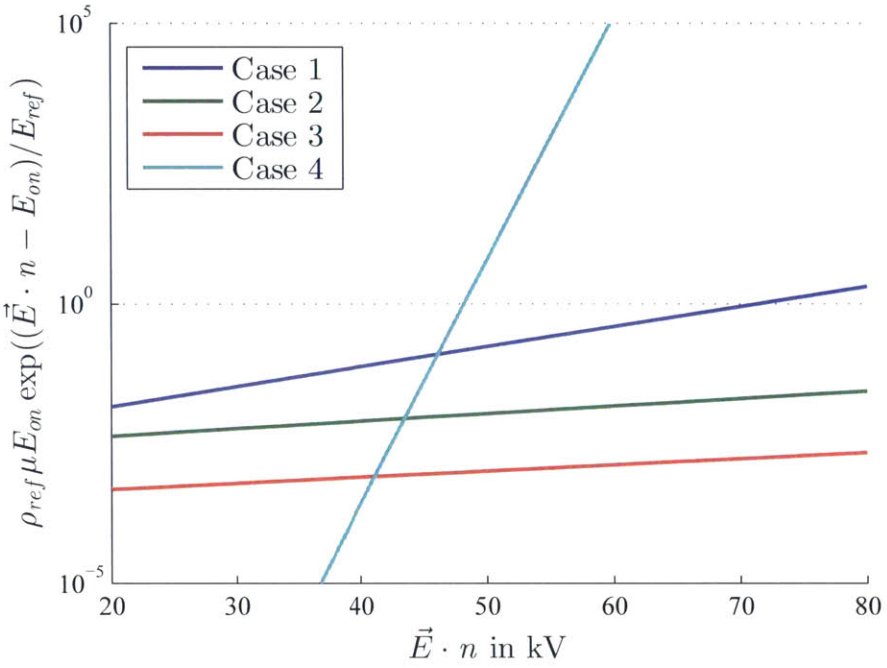


Figure 4-11: Charge injection term from equation (3.5) (see table 4.2 for cases).

Cases 1 through 3 for the charge injection parameters provide less variation in the required current density to satisfy equation (3.30) compared to case 4. The high sensitivity to the normal electric field provided by case 4 results in a closer approximation to the ideal charge injection boundary condition given by equation (3.29) at the expense of stability since the derivatives with respect to the normal electric field are very large.

The charge density corresponding to the cases in table 4.2 is assessed and solution parameters are examined at the emitter surface. The solution parameters are also evaluated for applied voltages ranging from 150 kV to 250 kV.

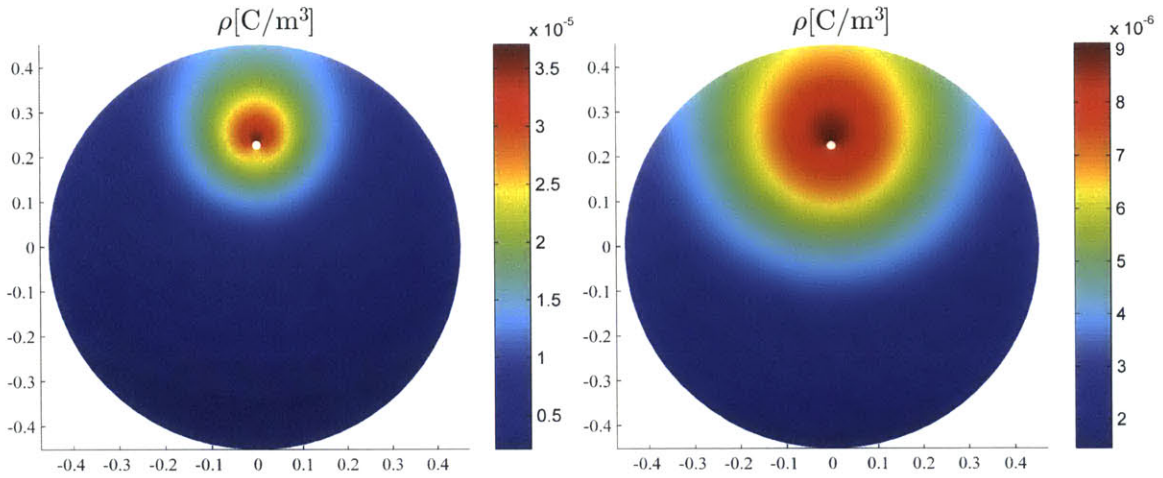


(a) $\rho_{ref} = 10^{-4}\,\mathrm{Cm}^{-3}$, $E_{ref} = 12.14\,{}^{\mathrm{kV}}/_{\mathrm{cm}}$. (b) $\rho_{ref} = 10^{-5}\,\mathrm{Cm}^{-3}$, $E_{ref} = 32.58\,{}^{\mathrm{kV}}/_{\mathrm{cm}}$.

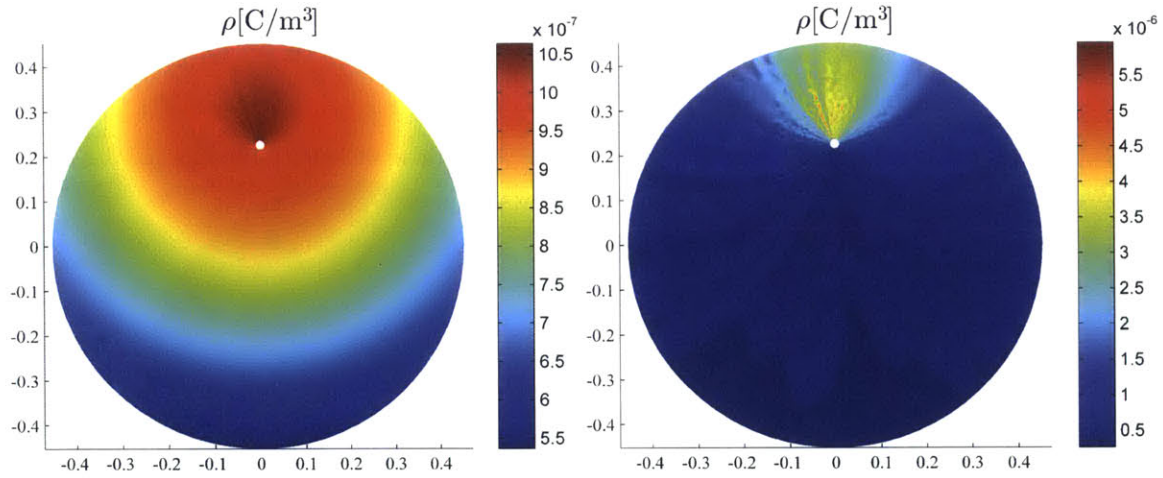


(c) $\rho_{ref} = 10^{-6}\,\mathrm{Cm}^{-3}$, $E_{ref} = 39.96\,{}^{\mathrm{kV}}/_{\mathrm{cm}}$. (d) $\rho_{ref} = 10^{-6}\,\mathrm{Cm}^{-3}$, $E_{ref} = 1\,{}^{\mathrm{kV}}/_{\mathrm{cm}}$.

Figure 4-12: Charge density solution using charge injection boundary condition, $\phi_0 = 150\,\mathrm{kV}$.

Figure 4-12 shows the charge density solution for each case from table 4.2. All solutions show that the charge density is greater in the smaller gap at 12 o'clock. The solution is also less uniform with evidence of ripples, particularly for case 4 shown in figure 4-12d. The ripples are indicative of numerical oscillations in the solution and are more visible as $\rho_{ref}$ is reduced. A finer mesh would allow for better resolution of the charge density with the effect of reducing the ripples. A comparison of figures 4-12c and 4-12d indicates that a smaller $E_{ref}$ allows for more variation in charge density along the emitter surface. This is in effect a closer approximation of the ideal

charge injection boundary condition.

Figure 4-14 shows electric field, current density, and charge density on the emitter surface. The 12 o'clock position corresponds to location of the minimum gap between the emitter and the outer cylinder. All choices except case 4 for the charge injection parameters allow variation of the solution along the emitter surface. The electric field variation is the same for each case except that cases 3 and 4 drive the field strength closer to $E_{on}$. This is consistent with the fact that $\rho_{ref} = 10^{-6}\,\mathrm{Cm}^{-3}$ corresponds to the intersection with the $E_{on}$ line in figure 4-7a. Case 1 and 2 drive too much current injection such that the field is driven below $E_{on}$. Since $\rho_{ref}$ is the same for cases 3 and 4, the effect of $E_{ref}$ surmised previously is confirmed; the lower $E_{ref}$ drives higher sensitivity to the normal electric field resulting in greater variation in emitted current along the surface.

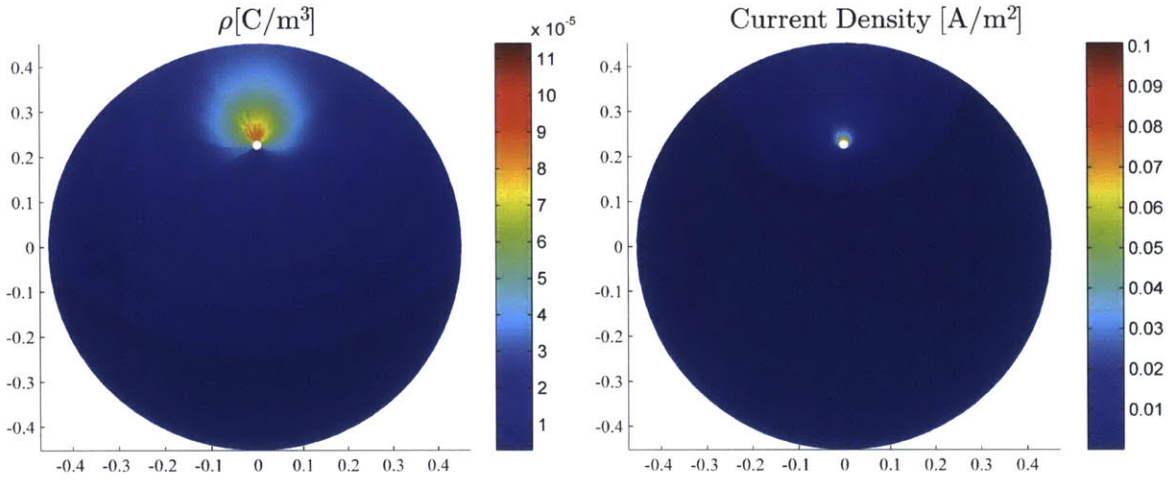


(a) Charge density.

(b) Current density.

Figure 4-13: Charge density and current density solution using charge injection boundary condition, $\rho_{ref} = 10^{-6}\,\mathrm{Cm}^{-3}$, $E_{ref} = 12.14\,^{\mathrm{kV}}/_{\mathrm{cm}}$, and $\phi_0 = 250\,\mathrm{kV}$.

Figure 4-15 is constructed similarly to figure 4-14 except the charge injection parameters are held constant at $\rho_{ref} = 10^{-6}\,\mathrm{Cm}^{-3}$ and $E_{ref} = 12.14\,^{\mathrm{kV}}/_{\mathrm{cm}}$ and the applied voltage $\phi_0$ is varied from 150 kV to 250 kV. The solution parameters do exhibit more variation along the boundary and due to the lower choice of $E_{ref}$. Some instability is evident with ripples on the boundary and in the domain shown in figure 4-13. While increasing $\phi_0$ does drive up the emitted current, the effect is not lin-

ear. Figure 4-15a shows that for the same increase in potential, the increase in field strength is reduced from 10% for case 1 to 2 to 2% for case 2 to 3.

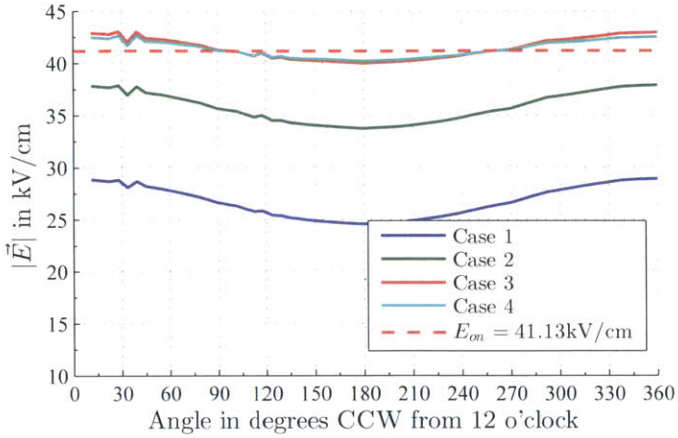


(a) Normal electric field.

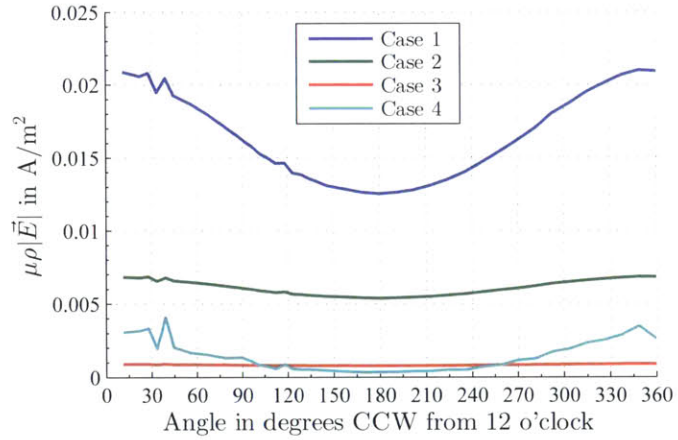


(b) Normal current density.

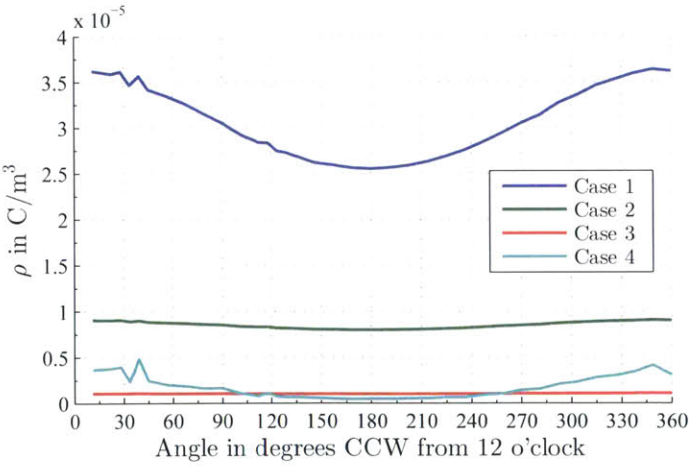


(c) Charge density.

Figure 4-14: Electric field, current density, and charge density along the emitter surface, $\phi_0 = 150\,\text{kV}$ (see table 4.2 for cases).

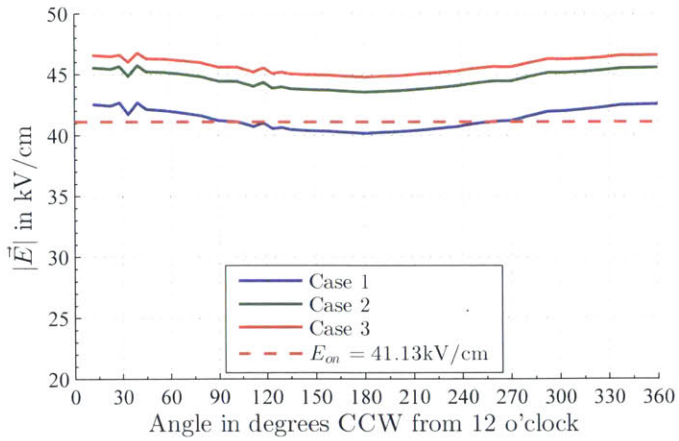


(a) Normal electric field.

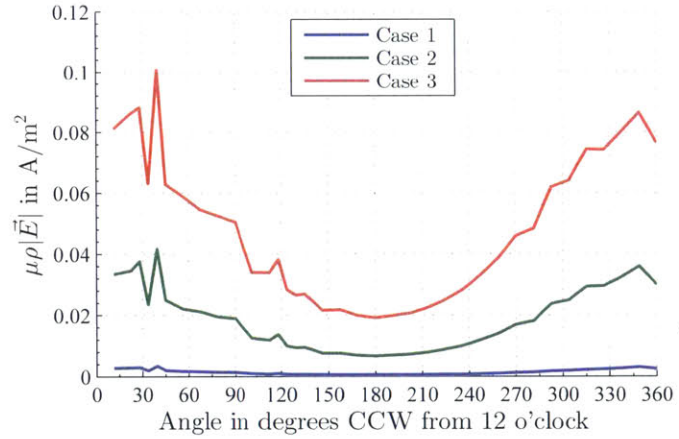


(b) Normal current density.

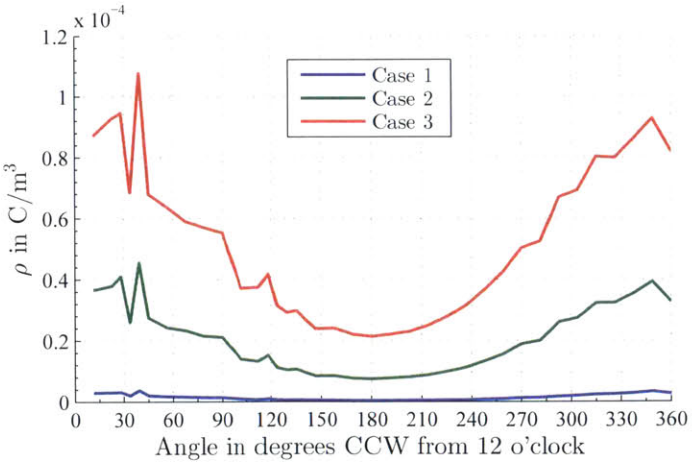


(c) Charge density.

Figure 4-15: Electric field, current density, and charge density along the emitter surface, $\rho_{ref} = 10^{-6}\,\mathrm{Cm}^{-3}$ and $E_{ref} = 12.14\,{}^{\mathrm{kV}}/_{\mathrm{cm}}$; cases correspond to $\phi_0 = 150\,\mathrm{kV}$, $200\,\mathrm{kV}$, and $250\,\mathrm{kV}$.

## 4.2 Single Stage Thruster

The single stage thruster is modeled using the natural boundary condition on domain edges, a charge injection boundary condition on the emitter, and an outflow boundary condition on the collector. The potential of the collector is held at zero while the potential applied to the emitter, $\phi_0$, is varied. The charge injection boundary condition is either a homogeneous current flux based on experimental measurements from Masuyama & Barrett [29, 30] or the charge injection model with parameters $\rho_{ref} = 10^{-4}\,\mathrm{Cm}^{-3}$ and $E_{ref} = 100\,{}^{\mathrm{kV}}/_{\mathrm{cm}}$. The large $E_{ref}$ facilitates convergence given the relatively coarse nature of the mesh. A denser mesh with 11428 elements allows for convergence of a high sensitivity charge injection boundary condition with $\rho_{ref} = 10^{-5}\,\mathrm{Cm}^{-3}$ and $E_{ref} = 1\,{}^{\mathrm{kV}}/_{\mathrm{cm}}$ but requires the use of a more powerful computer.

Contour plots of the solution for the homogeneous charge injection boundary condition are shown in figure 4-17. Corresponding plots for the charge injection model are shown in figure 4-18. The primary difference in the results is the magnitude of the charge density. The homogeneous case results in charge density on the order of $10^{-3}$ whereas the charge injection model results in charge density a full order of magnitude lower. The smoother charge injection characteristic does not drive enough of an increase in current for a given voltage. The charge density solution in Figure 4-16 is calculated with a higher sensitivity charge injection model on the coarse mesh. Even at a lower applied voltage, the solution exhibits faceting and numerical instability. Increased mesh density is required to use the less stable model.

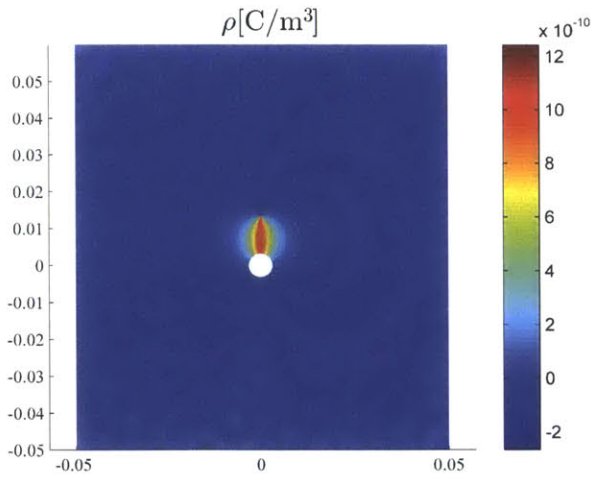


Figure 4-16: Charge density solution with charge injection boundary condition $\rho_{ref} = 10^{-5}\,\mathrm{Cm}^{-3}$ and $E_{ref} = 1\,{}^{\mathrm{kV}}/_{\mathrm{cm}}$ on the coarse mesh.

The post-processed thrust and current characteristics are compared to the experimental result from Masuyama & Barrett [29, 30] and 1D theory in figure 4-19. The homogeneous boundary condition case results in a maximum thrust error of 14%. This is likely due to the natural boundary condition applied to the domain boundary. The natural condition forces all emitted current to the collector; no charge escapes to the surrounding. Figure 4-20 compares the collected and emitted current for all analysis models. Figure 4-19b also confirms that the emitted current for the homogeneous boundary condition case exactly matches the imposed experimental results.

The low sensitivity charge injection case does not represent the experimental results very well. The maximum error in thrust is 75% and the maximum error in current is 76%. The model results in high current below the corona ignition voltage and low current at high voltages. The higher sensitivity charge injection model (noted as case 2 in figure 4-19) correlates better with the experimental results but does not converge on the coarse mesh at higher voltages. The maximum thrust error is 0.4 mN with a current error of $1.8 \times 10^{-7}$ mA. The experimentally measured current was zero with a non-zero thrust; this indicates that the current level is below the measurement resolution. The high resolution mesh allows the high sensitivity charge injection case to converge properly at higher applied voltages. The thrust and current characteristics (see case 3 in figure 4-19) are within 6% of the homogeneous case and within 19%

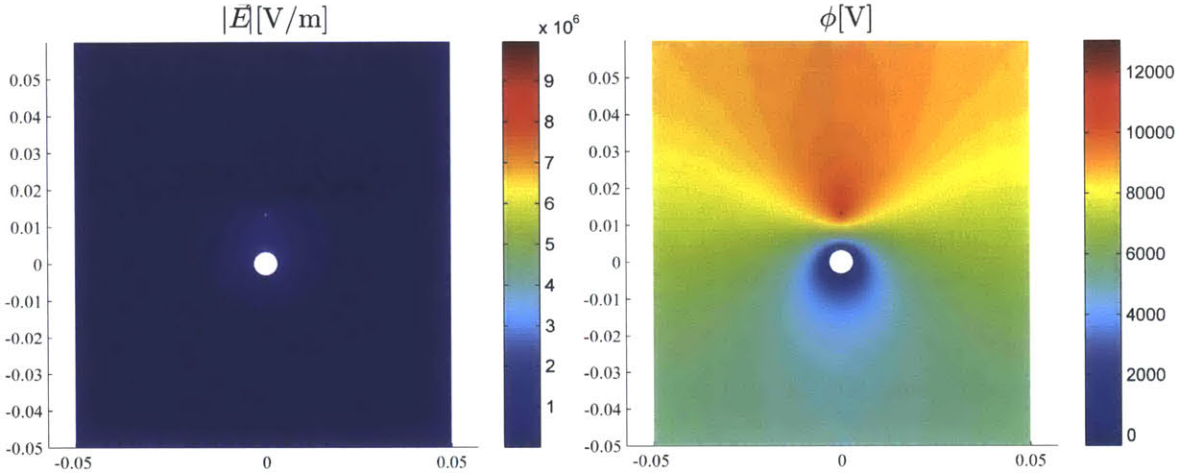


(a) Electric field.

(b) Electric potential.

(c) Charge density.

(d) Current density.

Figure 4-17: Solution using homogeneous charge injection boundary condition with $I_m = 0.46\,\text{mA}$, $\phi_0 = 13\,\text{kV}$.

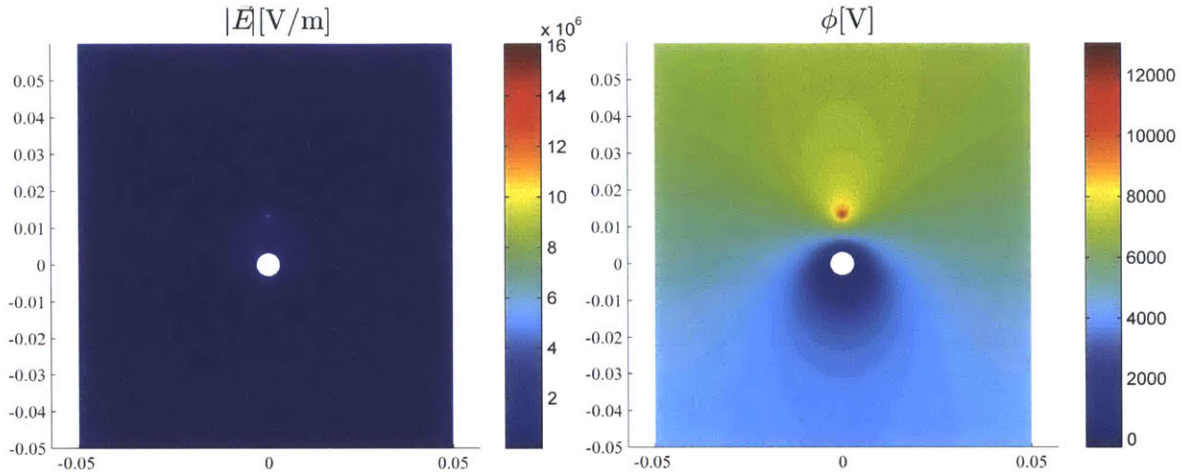


(a) Electric field.

(b) Electric potential.

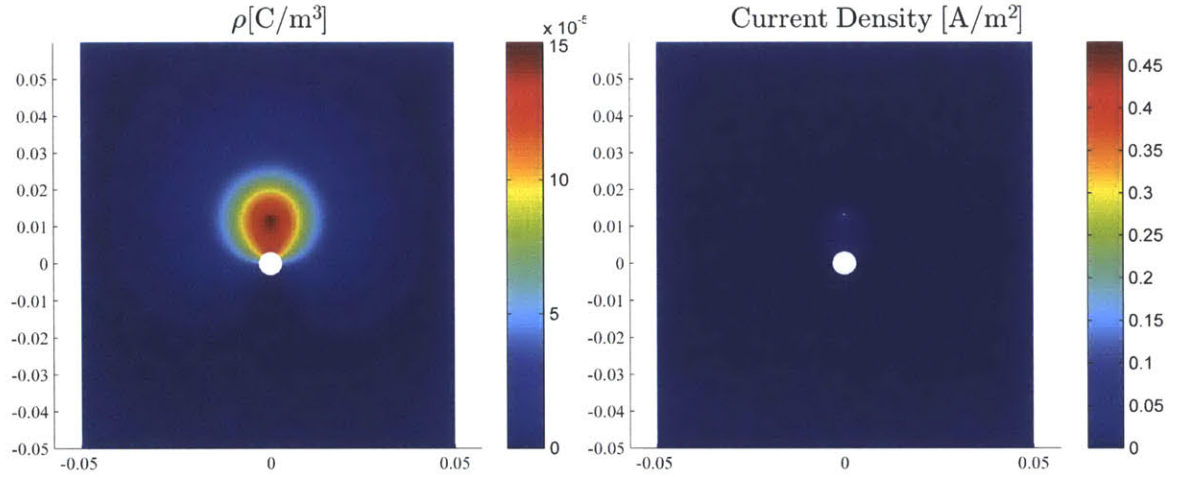


(c) Charge density.

(d) Current density.

Figure 4-18: Solution using charge injection boundary condition $\rho_{ref} = 10^{-4}\,\mathrm{Cm}^{-3}$ and $E_{ref} = 100\,{}^{\mathrm{kV}}/_{\mathrm{cm}}$, $\phi_0 = 13\,\mathrm{kV}$.

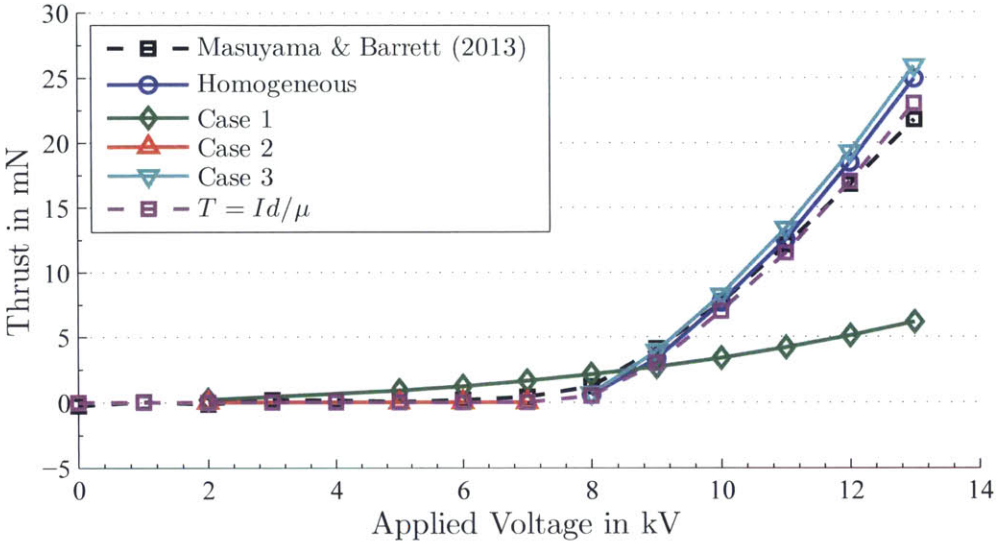


(a) Thrust-voltage characteristic.

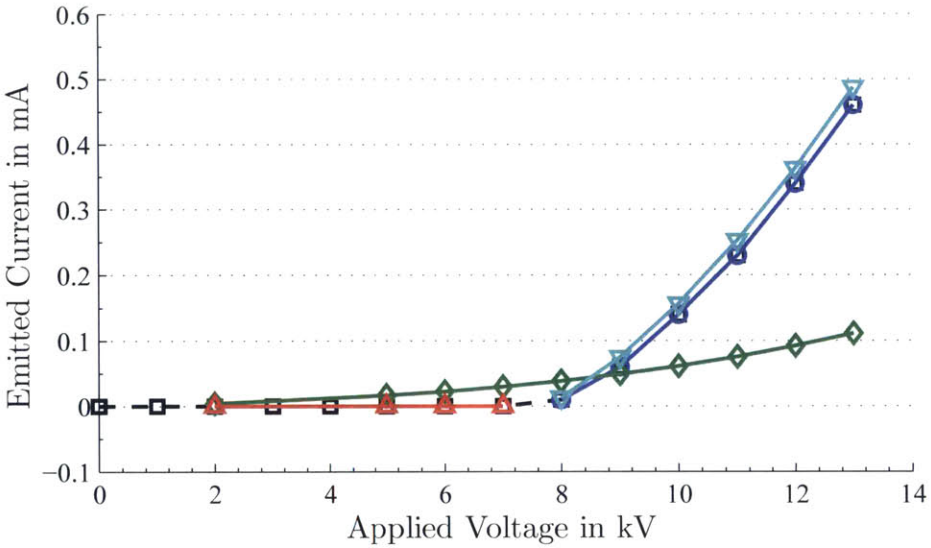


(b) Current-voltage characteristic.

Figure 4-19: Thrust and current characteristics compared to experimental data and 1D theory. Experimental currents are applied to the emitter for the homogeneous case. Charge injection boundary condition cases: 1) $\rho_{ref} = 10^{-4}\,\mathrm{Cm}^{-3}$, $E_{ref} = 100\,{}^{\mathrm{kV}}/_{\mathrm{cm}}$, 2) $\rho_{ref} = 10^{-5}\,\mathrm{Cm}^{-3}$, $E_{ref} = 1\,{}^{\mathrm{kV}}/_{\mathrm{cm}}$ on coarse mesh, 3) $\rho_{ref} = 10^{-5}\,\mathrm{Cm}^{-3}$, $E_{ref} = 1\,{}^{\mathrm{kV}}/_{\mathrm{cm}}$ on fine mesh.

of the experimental results and 1D theory. These results demonstrate the predictive capability of the charge injection model.

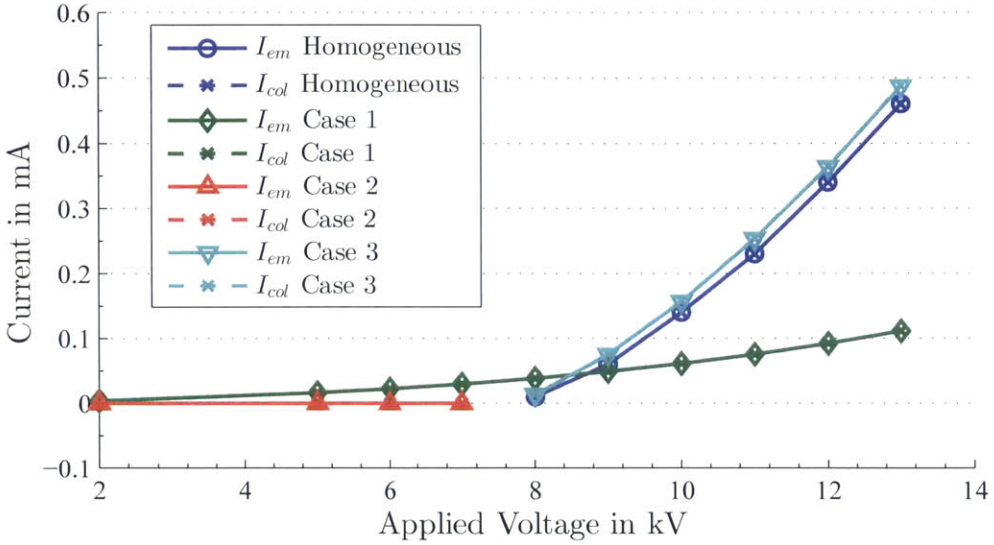


Figure 4-20: Emitted and collected current for homogeneous boundary condition and charge injection boundary condition cases: 1) $\rho_{ref} = 10^{-4}\,\mathrm{Cm}^{-3}$, $E_{ref} = 100\,{}^{\mathrm{kV}}/_{\mathrm{cm}}$, 2) $\rho_{ref} = 10^{-5}\,\mathrm{Cm}^{-3}$, $E_{ref} = 1\,{}^{\mathrm{kV}}/_{\mathrm{cm}}$ on coarse mesh, 3) $\rho_{ref} = 10^{-5}\,\mathrm{Cm}^{-3}$, $E_{ref} = 1\,{}^{\mathrm{kV}}/_{\mathrm{cm}}$ on fine mesh.

Electric field strength, charge density, and current density on the surface of the emitter for the homogeneous, low sensitivity charge injection, and high sensitivity charge injection boundary condition cases are shown in figure 4-21. The homogeneous boundary condition results in constant current density. The charge density varies around the perimeter inversely to the electric field strength. The field strength from the homogeneous boundary condition case is 20% lower than the critical value $E_{on}$. This indicates that either Peek's law does not accurately predict the critical field strength or the 2D model does not capture some 3D corona discharge effects. The surface condition parameter used in Peek's law to calculate the critical field strength is $m_s = 1$. A different choice of $m_s$ could result in a closer match to the experimental results.

The high sensitivity charge injection case drives the electric field strength to within 5% of the critical value. Charge density at the surface of the emitter exhibits far more variation around the circumference compared to the lower sensitivity charge injection

case with a peak at the 6 o'clock position. This corresponds to the location of highest electric field strength. The jagged charge density trace is indicative of the instability inherent in the high sensitivity charge injection boundary condition parameters.

Corresponding plots for the collector electrode are shown in figure 4-22c. The current is collected primarily on the upper half of the collector. The critical field strength for the collector is $E_{on} = 46.64\,{}^{\mathrm{kV}}/_{\mathrm{cm}}$. The maximum field strength on the collector is less than half of the critical value; this indicates that a negative corona at the collector is not likely.

While the low sensitivity charge injection results presented here do not reproduce the experimental results, the fact that the high sensitivity model is a better match indicates that the charge injection model is tunable to balance accuracy and solution stability. The stability of the model will increase with mesh density since the sharper changes in current flux can be more accurately represented. The present study is limited by the resources available on a personal computer or desktop. A mainframe or server would be required to perform computations for larger models.

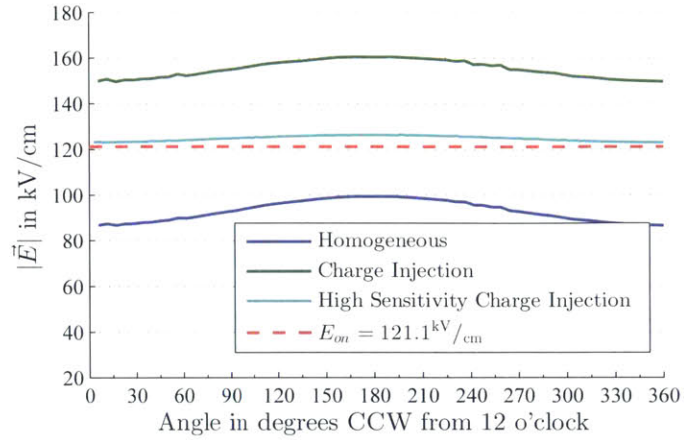


(a) Electric field.

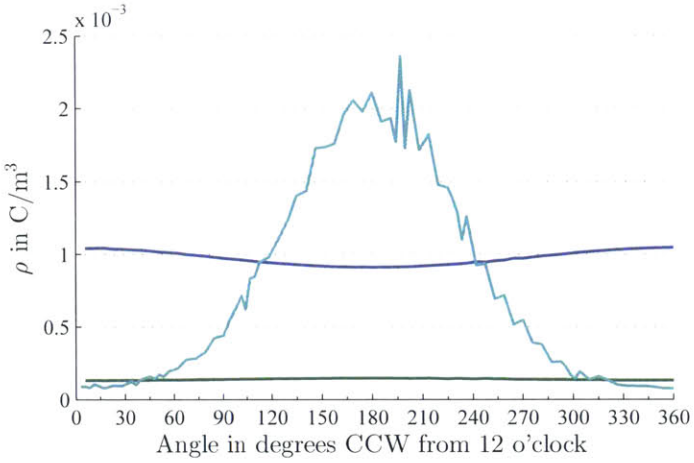


(b) Charge density.

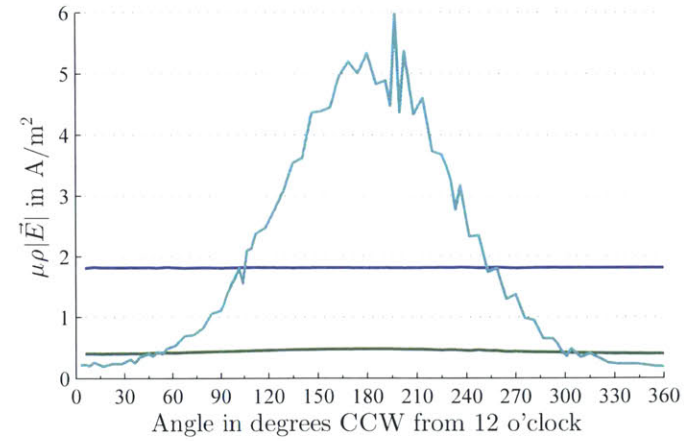


(c) Current density.

Figure 4-21: Electric field strength, charge density, and current density on the emitter surface, $\phi_0 = 13\,\mathrm{kV}$. The charge injection settings are $\rho_{ref} = 10^{-4}\,\mathrm{Cm}^{-3}$, $E_{ref} = 100\,^{\mathrm{kV}}/_{\mathrm{cm}}$ and $\rho_{ref} = 10^{-5}\,\mathrm{Cm}^{-3}$, $E_{ref} = 1\,^{\mathrm{kV}}/_{\mathrm{cm}}$ for the high sensitivity case.

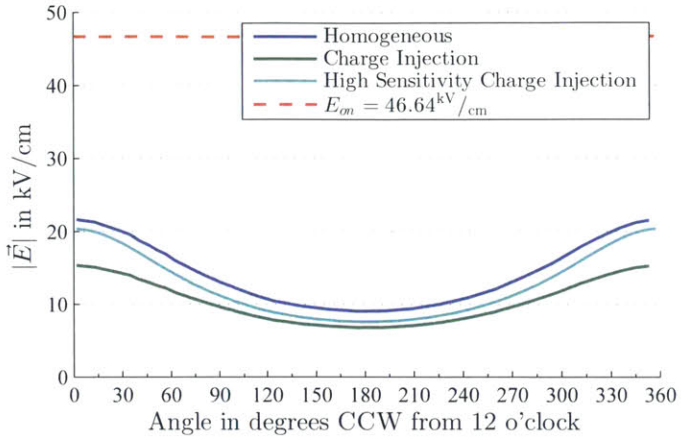


(a) Electric field.

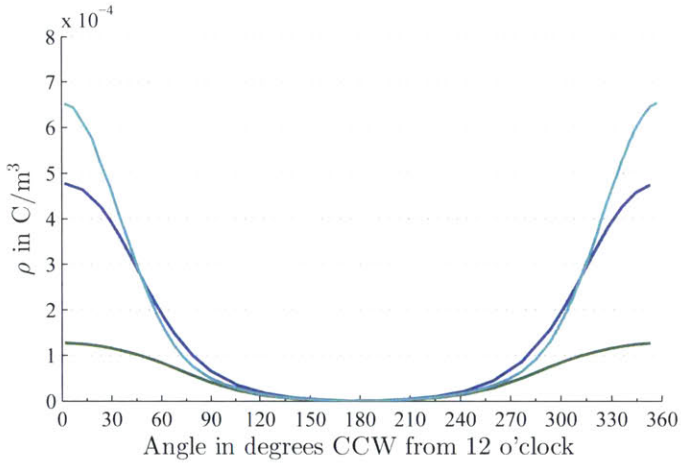


(b) Charge density.

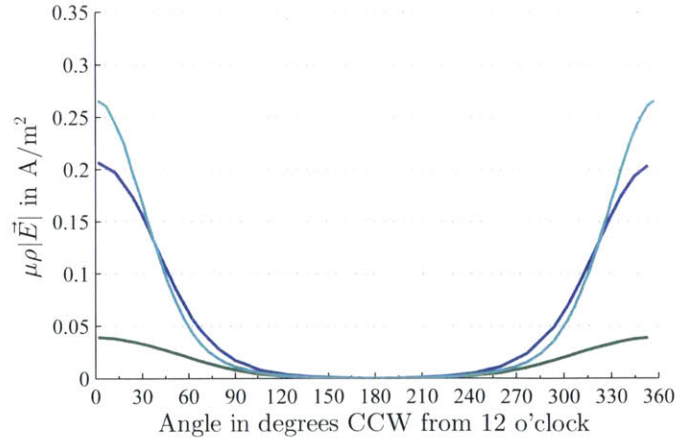


(c) Current density.

Figure 4-22: Electric field strength, charge density, and current density on the collector surface, $\phi_0 = 13\,\mathrm{kV}$. The charge injection settings are $\rho_{ref} = 10^{-4}\,\mathrm{Cm}^{-3}$, $E_{ref} = 100\,^{\mathrm{kV}}/_{\mathrm{cm}}$ and $\rho_{ref} = 10^{-5}\,\mathrm{Cm}^{-3}$, $E_{ref} = 1\,^{\mathrm{kV}}/_{\mathrm{cm}}$ for the high sensitivity case.

## 4.3 Dual Stage Thruster

The dual stage thruster model takes advantage of the system's vertical symmetry to reduce the size of the problem. An experimentally determined current from Masuyama & Barrett [29,30] for $V_1 = 5\,\mathrm{kV}$ is applied as a homogeneous current injection boundary condition the emitter. The HDG formulation presented in the current work is unable to arrive at a converged solution. The un-converged charge density and potential are shown in figure 4-23. The charge density solution exhibits faceting due to numerical instability. A stream of charge is also evident in the gap between the intermediate electrode and the collector. This stream of charge is not physical and is a product of the outflow boundary condition applied to the intermediate and collecting electrode. The outflow boundary condition given by equation (3.26) allows any incoming current flux. Current stream-tubes bounded by field lines emanating from the intermediate electrode and terminating on the collector can thus contain an arbitrary current. The problem becomes ill-posed since the solution for charge density is not unique.

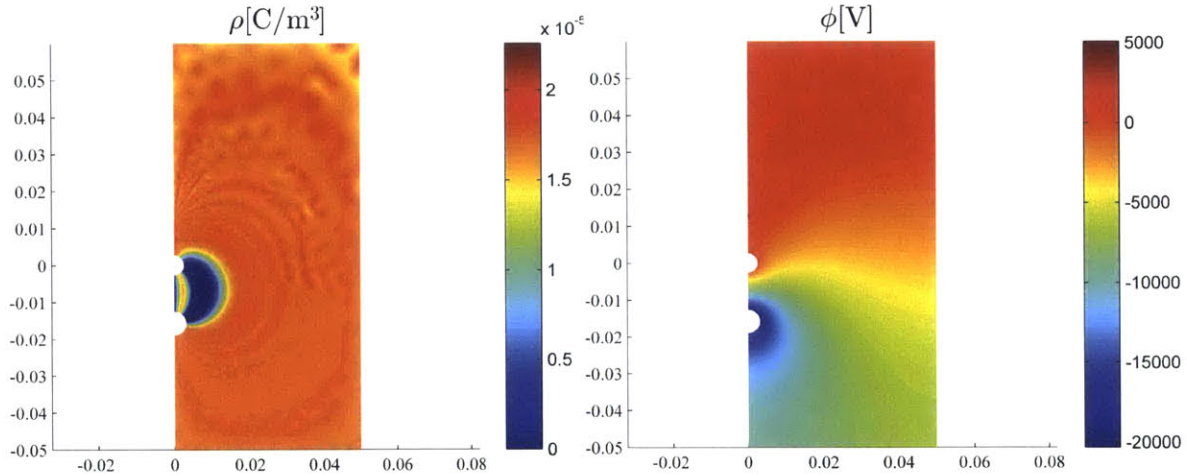


(a) Charge density solution. (b) Potental solution.

Figure 4-23: Un-converged potential and charge density solution using $\phi_0 = 5\,\mathrm{kV}$ and experimentally determined current 0.015 mA from Masuyama & Barrett [29, 30].

A more appropriate boundary condition for the intermediate electrode is a mixed boundary condition. A mixed boundary condition allows current outflow on the

portion of the boundary where $\vec{E} \cdot \boldsymbol{n} < 0$ and requires a Dirichlet boundary condition, $\rho = 0$, everywhere else. Implementing such a mixed boundary condition becomes problem specific since the portion of boundary where the Dirichlet condition applies is not known a priori. The mesh must also be sufficiently dense to allow resolution of the transition from the outflow portion of the boundary to the Dirichlet portion.

The mixed boundary condition is not novel. Cagnoni et al. [4] did include it as part of the requirements for discharging electrodes in their study, however, the geometries they investigated did not include a configuration which allows charge stream-tubes between non-emitting surfaces. The geometry modeled by Martins [27] does allow for such a situation but he avoids the problem by applying a zero charge Dirichlet condition to the collecting electrodes. This approach is less physically accurate and may introduce errors into the results.

# Chapter 5

# Conclusions

This thesis presents an HDG formulation and numerical scheme for solving the EHD thruster governing equations. The approach is used with a model problem, a single stage thruster geometry, and a dual stage thruster geometry to assess solution accuracy and performance. The validation analysis shows that the scheme accurately solves the governing equations and replicates test results when using a posteriori charge injection boundary conditions. A predictive charge injection boundary condition poses numerical challenges which require more computing resources to improve accuracy.

The HDG scheme implemented here successfully solves the governing equations within a normalized error on the order of $10^{-3}$ for second order elements. Further, the solution is achieved with less than 10 Newton iterations. The number of solution iterations is reduced if the initial solution is close to the final solution. The convergence rate for the potential solution is better than second order and variable with each iteration. The convergence rate for the charge density can be as good as second order.

The ideal charge injection boundary condition was not implemented since it always allows the trivial solution. The CG-FEM implementation by Feng [13] required additional residual equations to avoid this problem. The charge injection boundary condition model proposed by Cagnoni et al. [4] is used instead. The model does not allow the trivial solution and is tunable to balance stability and accuracy via the

choice of reference parameters.

The charge injection model is shown to qualitatively approximate the expected variation of charge and normal electric field on the emitting electrode. The model problem geometry with an offset emitter shows that the charge injection model biases the current flux to the area of the emitter with the highest electric field. The model does not strictly enforce Kaptsov's hypothesis that the electric field is pinned at the critical value at the emitter. This affects the predictive capability of model.

Analysis of the single stage thruster using the predictive charge injection model shows that the model can predict the thruster performance if higher sensitivity parameters are chosen. The solution does not converge on the coarse mesh at higher applied voltages. Lower sensitivity settings allow convergence at the expense of predictive accuracy. Higher sensitivity settings on a fine mesh allow predictive simulations with thrust and current errors up to 19% of the experimentally measured values.

If experimentally determined currents are used, the HDG model reproduces the measured thrust within 14% error. The discrepancy could be due to the natural boundary condition applied to the domain. All emitted current is forced to the collector which would result in higher thrust since more charge is available to impose a Coulomb force on the electrodes. The model results also show that the the critical field strength is not maintained at the emitter. This indicates that Peek's law should be modified with a surface factor less than one for this geometry or that there are 3D discharge effects that are not captured in the model.

The ability of this model to reproduce the experimental results is encouraging given that the analysis models in the literature are much larger. The geometry analyzed by Martins & Pinheiro [27] and Martins [28] required meshes with more than $50,000$ elements. An HDG problem size beyond 5000 second order elements becomes cumbersome on a personal computer in terms of computing time and memory resources.

The attempt at modeling the dual stage thruster illustrates a shortfall of the current HDG implementation. The charge outflow boundary condition allows non-unique solutions in charge stream-tubes connecting outflow surfaces. This situation

occurs between the intermediate and the collector in the dual stage thruster geometry. A mixed boundary condition is required to address this problem. Other geometries modeled in the literature generally do not allow this indeterminate situation. Martins [27] avoided this problem by applying Dirichlet boundary conditions.

## 5.1 Recommendations for Future Work

This work constitutes a first step in developing an HDG based solver for analyzing the electrohydrodynamic phenomenon associated with EHD propulsion devices. It is, in effect, a numerical proof on concept. There are a number of additional steps to move beyond this basic implementation to arrive at a full fledged design tool.

The most significant omission in the HDG approach shown here is the lack of fluid effects. The HDG approach has been successfully applied to a variety of fluid problems by Nguyen & Peraire [36]. The theoretical formulation must be revisited to include fluid parameters from the Navier-Stokes equations. The resulting problem size will be impractical to solve on a personal computer. An intermediate measure could utilized readily available N-S analysis codes like OpenFOAM to solve the flow equations with a linking approach like that used by Cagnoni et al. [4].

In anticipation of larger and more complex problems, a parallel computing implementation should be explored. Such an implementation should take advantage of networked computing resources to allow distributed batch processing of problems. The implementation should be accelerated using compiled functions as well to improve solution time speed.

The errors in replicating experimental results are related to boundary conditions. The accuracy of the high sensitivity charge injection boundary condition should be investigated using fine meshes to confirm the solution convergence which is observed with lower sensitivity implementations. The charge outflow boundary condition should be revised to allow for a mixed boundary condition for appropriate electrodes. This effort is likely to be numerically challenging since an adaptive mesh may be required to resolve the transition from outflow to Dirichlet boundary conditions. Fi-

nally, a representative open domain boundary condition should be developed for the HDG method. An approach similar to the ballooning boundary analysis presented by Silvester & Hsieh [47] could be fruitful. Another facet of the HDG approach that is not implemented here is the elemental post-processing which allows for $H(\mathbf{div}, \Omega)$ conforming solutions. In practice, this serves to improve solution accuracy and convergence rate [37–39]. Including elemental post-processing between each Newton iteration may alleviate some of the instability introduced with a high sensitivity charge injection boundary condition.

# Appendix A

# HDG for Poisson Equation

An abbreviated presentation of the HDG formulation for the Poisson problem is shown here. The solution found using this approach is used to initialize the solution for the full set of nonlinear equations in chapter 3. For details beyond what is shown here, please see the work by Nguyen et al. [37].

The governing equation for the Poisson problem do not include the charge conservation equation. They are

$$\vec{E} + \nabla\phi = 0, \tag{A.1}$$

$$\nabla \cdot \vec{E} = \frac{\rho}{\epsilon_0}. \tag{A.2}$$

The function spaces and inner products are defined in the same way as shown in section 3.2.1 except the tensor space $\boldsymbol{\mathcal{Q}}_h^k$ is not required. The numerical flux is given by

$$\hat{\vec{E}}_h = \vec{E}_h - \tau(\phi_h - \hat{\phi}_h)\boldsymbol{n} \tag{A.3}$$

Multiplying (A.1) and (A.2) through by test functions and integrating by parts yields

$$\left(\vec{E}_h, \boldsymbol{a}\right)_{\mathcal{T}_h} - \left(\phi_h, \nabla \cdot \boldsymbol{a}\right)_{\mathcal{T}_h} + \left\langle \hat{\phi}_h, \boldsymbol{a} \cdot \boldsymbol{n} \right\rangle_{\partial\mathcal{T}_h} = 0, \tag{A.4}$$

$$-\left(\nabla \cdot \vec{E}_h, a\right)_{\mathcal{T}_h} + \left\langle \tau\phi_h, a \right\rangle_{\partial\mathcal{T}_h} - \left\langle \tau\hat{\phi}_h, a \right\rangle_{\partial\mathcal{T}_h} = \left(-\rho/\epsilon_0, a\right)_{\mathcal{T}_h}, \tag{A.5}$$

$$\left\langle \vec{E}_h \cdot \boldsymbol{n}, \mu \right\rangle_{\partial\mathcal{T}_h} - \left\langle \tau\phi_h, \mu \right\rangle_{\partial\mathcal{T}_h} + \left\langle \tau\hat{\phi}_h, \mu \right\rangle_{\partial\mathcal{T}_h} = \left\langle \boldsymbol{g}_N, \mu \right\rangle_{\mathcal{T}_h}. \tag{A.6}$$

Note that the numerical flux given by equation (A.3) has been substituted into the system. This is possible since the problem is linear. The resulting elemental matrix system has the form

$$\begin{bmatrix} \mathbb{A}_K & -\mathbb{B}_K & \mathbb{C}_K \\ -\mathbb{B}_K^T & \mathbb{D}_K & -\mathbb{E}_K \\ \mathbb{C}_K^T & \mathbb{E}_K^T & \mathbb{M}_K \end{bmatrix} \begin{bmatrix} \mathbb{Q}_K \\ \mathbb{U}_K \\ \hat{\mathbb{U}}_K \end{bmatrix} = \begin{bmatrix} 0 \\ \mathbb{F}_K \\ \mathbb{G}_K \end{bmatrix} \tag{A.7}$$

The upper left quadrant is again block diagonal and may be inverted to reduce the system to degrees of freedom on the boundaries. Note that the system in this case has fewer unique sub-matrices. This facilitates matrix assembly by reducing required computations. The final form of the global problem is

$$\mathbb{H}\hat{\mathbb{U}} = \mathbb{R}. \tag{A.8}$$

Newton iterations are not required since the problem is linear. The accuracy of the solution is then limited by the mesh and element order.

# Appendix B

# Sensitivity Functions

This section provides details of the sensitivity functions used in the formulation shown in chapter 3. The flux sensitivities are shown first followed by the boundary condition sensitivities. The flux definitions are reproduced here for reference.

$$\boldsymbol{F} = \begin{pmatrix} \vec{E} \\ D\vec{C} + \mu\rho\vec{E} \end{pmatrix} \tag{B.1}$$

$$\hat{\boldsymbol{F}}_h = \boldsymbol{F}(\boldsymbol{Q}_h, \hat{\boldsymbol{u}}_h) - \tau(\boldsymbol{u}_h - \hat{\boldsymbol{u}}_h)\boldsymbol{n}, \tag{B.2}$$

The 2×2 matrices shown on the RHS in (B.3) are the derivatives of the components of $\boldsymbol{F}$ with respect to component $\boldsymbol{Q}_{(ij)}$. This convention is used for all sensitivities shown here.

$$\begin{bmatrix} \frac{\partial \boldsymbol{F}}{\partial \boldsymbol{Q}_{(11)}} \\ \frac{\partial \boldsymbol{F}}{\partial \boldsymbol{Q}_{(12)}} \\ \frac{\partial \boldsymbol{F}}{\partial \boldsymbol{Q}_{(21)}} \\ \frac{\partial \boldsymbol{F}}{\partial \boldsymbol{Q}_{(22)}} \end{bmatrix} = \begin{bmatrix} \begin{bmatrix} 1 & 0 \\ \mu\rho & 0 \end{bmatrix} \\ \begin{bmatrix} 0 & 1 \\ 0 & \mu\rho \end{bmatrix} \\ \begin{bmatrix} 0 & 0 \\ D & 0 \end{bmatrix} \\ \begin{bmatrix} 0 & 0 \\ 0 & D \end{bmatrix} \end{bmatrix} \tag{B.3}$$

$$\begin{bmatrix} \frac{\partial \boldsymbol{F}}{\partial \boldsymbol{u}}(1) \\ \frac{\partial \boldsymbol{F}}{\partial \boldsymbol{u}}(2) \end{bmatrix} = \begin{bmatrix} \begin{bmatrix} 1 & 0 \\ 0 & 0 \end{bmatrix} \\ \begin{bmatrix} 0 & 0 \\ \mu E_x & \mu E_y \end{bmatrix} \end{bmatrix} \tag{B.4}$$

$$\begin{bmatrix} \frac{\partial \hat{\boldsymbol{F}}}{\partial \boldsymbol{Q}}(11) \\ \frac{\partial \hat{\boldsymbol{F}}}{\partial \boldsymbol{Q}}(12) \\ \frac{\partial \hat{\boldsymbol{F}}}{\partial \boldsymbol{Q}}(21) \\ \frac{\partial \hat{\boldsymbol{F}}}{\partial \boldsymbol{Q}}(22) \end{bmatrix} = \begin{bmatrix} \begin{bmatrix} 1 & 0 \\ \mu\hat{\rho} & 0 \end{bmatrix} \\ \begin{bmatrix} 0 & 1 \\ 0 & \mu\hat{\rho} \end{bmatrix} \\ \begin{bmatrix} 0 & 0 \\ D & 0 \end{bmatrix} \\ \begin{bmatrix} 0 & 0 \\ 0 & D \end{bmatrix} \end{bmatrix} \tag{B.5}$$

$$\begin{bmatrix} \frac{\partial \hat{\boldsymbol{F}}}{\partial \boldsymbol{u}}(1) \\ \frac{\partial \hat{\boldsymbol{F}}}{\partial \boldsymbol{u}}(2) \end{bmatrix} = \begin{bmatrix} \begin{bmatrix} -\tau n_x & -\tau n_y \\ 0 & 0 \end{bmatrix} \\ \begin{bmatrix} 0 & 0 \\ -\tau n_x & -\tau n_y \end{bmatrix} \end{bmatrix} \tag{B.6}$$

$$\begin{bmatrix} \frac{\partial \hat{\boldsymbol{F}}}{\partial \hat{\boldsymbol{u}}}(1) \\ \frac{\partial \hat{\boldsymbol{F}}}{\partial \hat{\boldsymbol{u}}}(2) \end{bmatrix} = \begin{bmatrix} \begin{bmatrix} \tau n_x & \tau n_y \\ 0 & 0 \end{bmatrix} \\ \begin{bmatrix} 0 & 0 \\ \mu E_x + \tau n_x & \mu E_y + \tau n_y \end{bmatrix} \end{bmatrix} \tag{B.7}$$

Equation (B.8) shows the source term sensitivity.

$$\begin{bmatrix} \frac{\partial \boldsymbol{s}}{\partial \boldsymbol{u}}(1) \\ \frac{\partial \boldsymbol{s}}{\partial \boldsymbol{u}}(2) \end{bmatrix} = \begin{bmatrix} \begin{bmatrix} 0 \\ 0 \end{bmatrix} \\ \begin{bmatrix} \frac{1}{\epsilon_0} \\ 0 \end{bmatrix} \end{bmatrix} \tag{B.8}$$

The following sensitivities are for the ideal and smoothed charge injection bound-

ary conditions as well as the outflow boundary condition. The boundary condition expressions are repeated from section 3.

Current and electric field outflow:

$$\hat{\boldsymbol{F}} \cdot \boldsymbol{n} = \boldsymbol{g}_N = \boldsymbol{F} \cdot \boldsymbol{n} \text{ on } \partial\Omega_N. \tag{B.9}$$

$$\begin{bmatrix} \frac{\partial \boldsymbol{g}_N}{\partial \boldsymbol{Q}}_{(11)} \\ \frac{\partial \boldsymbol{g}_N}{\partial \boldsymbol{Q}}_{(12)} \\ \frac{\partial \boldsymbol{g}_N}{\partial \boldsymbol{Q}}_{(21)} \\ \frac{\partial \boldsymbol{g}_N}{\partial \boldsymbol{Q}}_{(22)} \end{bmatrix} = \begin{bmatrix} \begin{bmatrix} n_x \\ \rho\mu n_x \end{bmatrix} \\ \begin{bmatrix} n_y \\ \rho\mu n_y \end{bmatrix} \\ \begin{bmatrix} 0 \\ Dn_x \end{bmatrix} \\ \begin{bmatrix} 0 \\ Dn_y \end{bmatrix} \end{bmatrix} \tag{B.10}$$

$$\begin{bmatrix} \frac{\partial \boldsymbol{g}_N}{\partial \boldsymbol{u}}_{(1)} \\ \frac{\partial \boldsymbol{g}_N}{\partial \boldsymbol{u}}_{(2)} \end{bmatrix} = \begin{bmatrix} \begin{bmatrix} 0 \\ 0 \end{bmatrix} \\ \begin{bmatrix} 0 \\ \mu\vec{E} \cdot \boldsymbol{n} \end{bmatrix} \end{bmatrix} \tag{B.11}$$

Note that the outflow condition for the electric field is not used in the current study.

Ideal charge injection:

$$\boldsymbol{F}_2 \cdot \boldsymbol{n} = \boldsymbol{g}_N = -\rho\mu E_{on} \text{ on } \partial\Omega_N, \tag{B.12}$$

$$\begin{bmatrix} \frac{\partial \boldsymbol{g}_N}{\partial \boldsymbol{Q}}_{(11)} \\ \frac{\partial \boldsymbol{g}_N}{\partial \boldsymbol{Q}}_{(12)} \\ \frac{\partial \boldsymbol{g}_N}{\partial \boldsymbol{Q}}_{(21)} \\ \frac{\partial \boldsymbol{g}_N}{\partial \boldsymbol{Q}}_{(22)} \end{bmatrix} = \begin{bmatrix} \begin{bmatrix} 0 \end{bmatrix} \\ \begin{bmatrix} 0 \end{bmatrix} \\ \begin{bmatrix} 0 \end{bmatrix} \\ \begin{bmatrix} 0 \end{bmatrix} \end{bmatrix} \tag{B.13}$$

$$\begin{bmatrix} \frac{\partial \boldsymbol{g}_N}{\partial \boldsymbol{u}}(1) \\ \frac{\partial \boldsymbol{g}_N}{\partial \boldsymbol{u}}(2) \end{bmatrix} = \begin{bmatrix} \begin{bmatrix} 0 \end{bmatrix} \\ \begin{bmatrix} -\mu E_{on} \end{bmatrix} \end{bmatrix} \tag{B.14}$$

Smoothed charge injection:

$$\boldsymbol{F}_2 \cdot \boldsymbol{n} = \boldsymbol{g}_N = \boldsymbol{F}_2 \cdot \boldsymbol{n} + \rho\mu E_{on} - \rho_{ref}\mu E_{on} \exp\left(\frac{-\vec{E} \cdot \boldsymbol{n} - E_{on}}{E_{ref}}\right) \text{ on } \partial\Omega_N. \tag{B.15}$$

Here the superscript (2) on the flux denotes the conservation of charge flux components.

$$\begin{bmatrix} \frac{\partial \boldsymbol{g}_N}{\partial \boldsymbol{Q}}(11) \\ \frac{\partial \boldsymbol{g}_N}{\partial \boldsymbol{Q}}(12) \\ \frac{\partial \boldsymbol{g}_N}{\partial \boldsymbol{Q}}(21) \\ \frac{\partial \boldsymbol{g}_N}{\partial \boldsymbol{Q}}(22) \end{bmatrix} = \begin{bmatrix} \begin{bmatrix} \frac{\partial \boldsymbol{F}^{(2)}}{\partial \boldsymbol{Q}}(11) \cdot \boldsymbol{n} - \rho_{ref}\mu E_{on} \exp((-\vec{E} \cdot \boldsymbol{n} - E_{on})/E_{ref}) \frac{-n_x}{E_{ref}} \end{bmatrix} \\ \begin{bmatrix} \frac{\partial \boldsymbol{F}^{(2)}}{\partial \boldsymbol{Q}}(12) \cdot \boldsymbol{n} - \rho_{ref}\mu E_{on} \exp((-\vec{E} \cdot \boldsymbol{n} - E_{on})/E_{ref}) \frac{-n_y}{E_{ref}} \end{bmatrix} \\ \begin{bmatrix} \frac{\partial \boldsymbol{F}^{(2)}}{\partial \boldsymbol{Q}}(21) \cdot \boldsymbol{n} \end{bmatrix} \\ \begin{bmatrix} \frac{\partial \boldsymbol{F}^{(2)}}{\partial \boldsymbol{Q}}(22) \cdot \boldsymbol{n} \end{bmatrix} \end{bmatrix} \tag{B.16}$$

$$\begin{bmatrix} \frac{\partial \boldsymbol{g}_N}{\partial \boldsymbol{u}}(1) \\ \frac{\partial \boldsymbol{g}_N}{\partial \boldsymbol{u}}(2) \end{bmatrix} = \begin{bmatrix} \begin{bmatrix} \frac{\partial \boldsymbol{F}^{(2)}}{\partial \boldsymbol{u}}(1) \cdot \boldsymbol{n} \end{bmatrix} \\ \begin{bmatrix} \frac{\partial \boldsymbol{F}^{(2)}}{\partial \boldsymbol{u}}(2) \cdot \boldsymbol{n} + \mu E_{on} \end{bmatrix} \end{bmatrix} \tag{B.17}$$

# Appendix C

# Integration Implementation

Numerical integration of the volume and surface inner products are achieved using the set of Koornwinder orthogonal basis functions. The code which calculates the value of the basis functions at points on the unit master element as well as the Gauss integration points and weights was provided by Jaime Peraire for the 16.930 course offered at MIT. Since the basis functions are defined on the master element, integrals for a given element must be mapped onto the master element using the Jacobian matrix

$$J = \begin{bmatrix} \frac{\partial x}{\partial \xi} & \frac{\partial y}{\partial \xi} \\ \frac{\partial x}{\partial \eta} & \frac{\partial y}{\partial \eta} \end{bmatrix}. \tag{C.1}$$

A volume integral can then be computed by

$$\int_K f(u_h(\boldsymbol{x}), \boldsymbol{x})\phi_i\phi_j = \sum_{n=1}^{N^g} W_n^g f(u_h(\boldsymbol{x}_n^g), \boldsymbol{x}_n^g)\phi_i(\boldsymbol{\xi}_n^g)\phi_j(\boldsymbol{\xi}_n^g)|J|, \tag{C.2}$$

where $\boldsymbol{\xi}_n^g$ are the Gauss points and $W_n^g$ are the Gauss weights. A face integral is constructed in a similar manner, however, the Jacobian matrix is reduced to the face by defining

$$|I| = \sqrt{\left(\frac{\partial y}{\partial \xi}\right)^2 + \left(\frac{\partial x}{\partial \xi}\right)^2}, \tag{C.3}$$

where $\xi$ is the coordinate along a unit line. The face integral is mapped onto a unit line "master element". The tangential vector and normal are given respectively by

$$\boldsymbol{\tau} = \frac{1}{|I|}\left(\frac{\partial x}{\partial \xi}, \frac{\partial y}{\partial \xi}\right), \tag{C.4}$$

$$\boldsymbol{n} = \frac{1}{|I|}\left(\frac{\partial y}{\partial \xi}, \frac{-\partial x}{\partial \xi}\right). \tag{C.5}$$

A face integral can then by computed by

$$\int_F f(u_h(\boldsymbol{x}), \boldsymbol{x}) n_x \phi_i \phi_j = \sum_{n=1}^{M^g} \overline{W}_n^g f(u_h(\bar{\boldsymbol{x}}_n^g), \bar{\boldsymbol{x}}_n^g) n_x(\bar{\boldsymbol{x}}_n^g) \phi_i(\bar{\xi}_n^g) \phi_j(\bar{\xi}_n^g) |I(\bar{\xi}_n^g)|, \tag{C.6}$$

where $\bar{\xi}_n^g$ are the Gauss points and $M_n^g$ are the Gauss weights.

# Appendix D

# Analysis Meshes

The analysis meshes used for each validation problem in chapter 4 are shown here. The mesh size is limited to less than 4000 elements to facilitate solving on a personal computer.

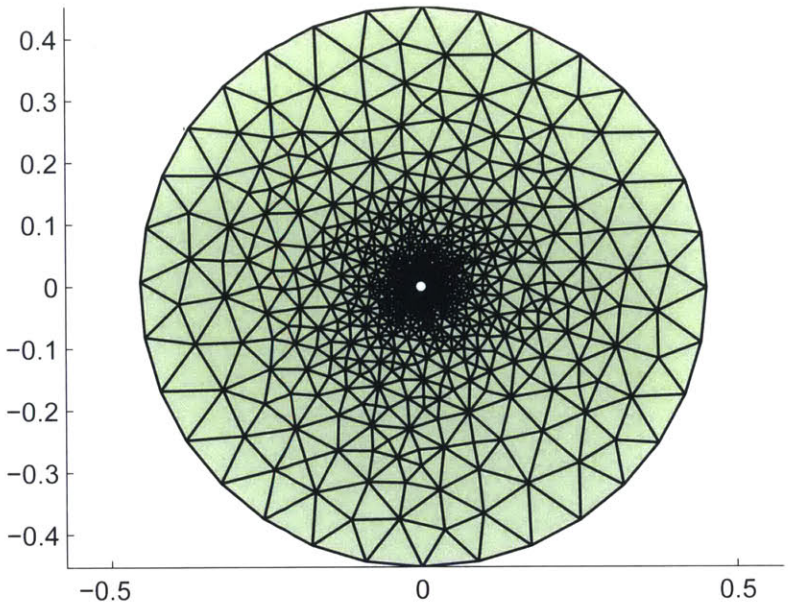


Figure D-1: Model problem mesh, 1564 elements.

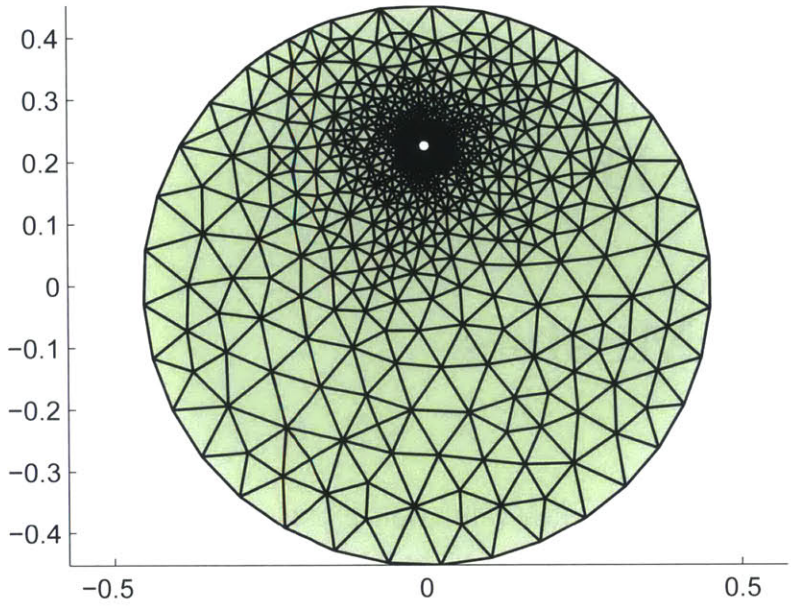


Figure D-2: Model problem mesh with offset emitter, 1564 elements.

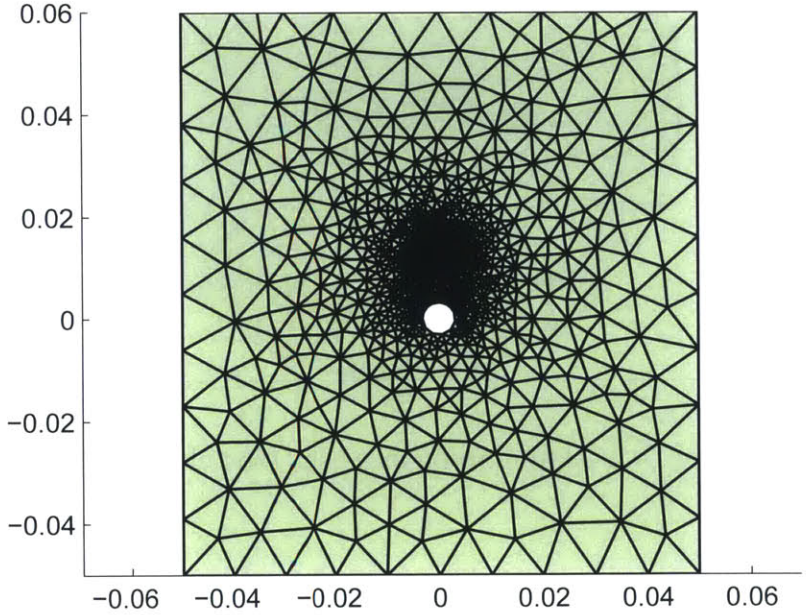


Figure D-3: Single stage thruster mesh, 3746 elements.

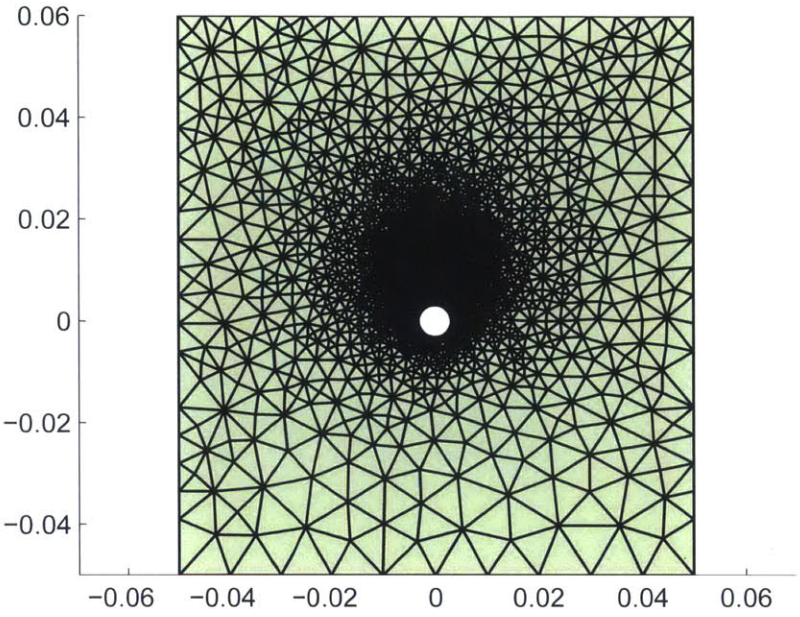


Figure D-4: Single stage thruster mesh, 11428 elements.

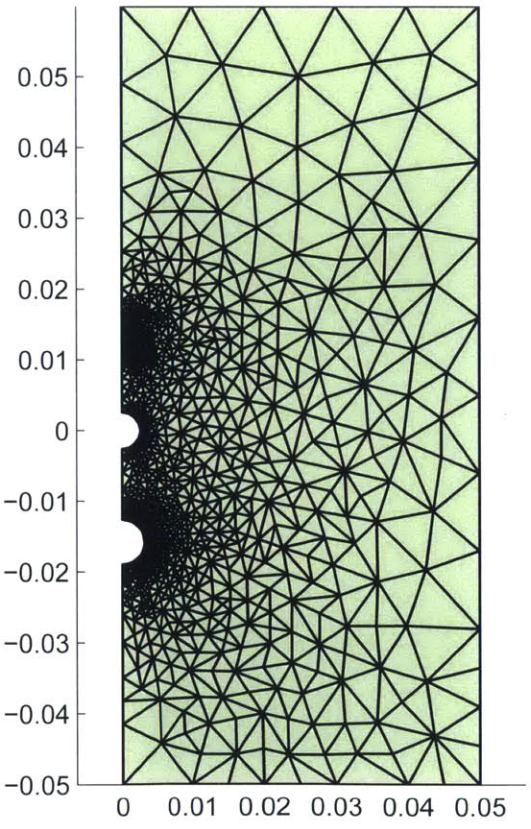


Figure D-5: Dual stage thruster mesh, 2355 elements.

# Nomenclature

| | |
|---|---|
| CG | Continuous Galerkin |
| DG | Discontinuous Galerkin |
| EHD | Electrohydrodynamic |
| FE | Finite Element |
| HDG | Hybridized Discontinuous Galerkin |

**Constants**

| | | |
|---|---|---|
| $\epsilon_0$ | Permitivity of free space | $\approx 8.854 \times 10^{-12}\,\frac{\mathrm{F}}{\mathrm{m}}$ |
| $k_b$ | Boltzmann constant | $\approx 1.3806 \times 10^{-23}\,\frac{\mathrm{J}}{\mathrm{K}}$ |
| $q$ | Elementary charge | $\approx 1.602 \times 10^{-16}\,\mathrm{C}$ |

**Variables**

| | | |
|---|---|---|
| $\mu$ | Ion mobility | $\frac{\mathrm{m}^2}{\mathrm{Vs}}$ |
| $\phi$ | Electric potential | V |
| $\rho$ | Charge density | $\frac{\mathrm{C}}{\mathrm{m}^3}$ |
| $\vec{C}$ | Gradient of charge density | $\frac{\mathrm{C}}{\mathrm{m}^4}$ |
| $\vec{E}$ | Electric field | $\frac{\mathrm{V}}{\mathrm{m}}$ |
| $\vec{B}$ | Magnetic field | T |

| | | |
|---|---|---|
| $\vec{j}$ | Current density | $\frac{\mathrm{A}}{\mathrm{m}^2}$ |
| $\vec{u}$ | Velocity field | $\frac{\mathrm{m}}{\mathrm{s}}$ |
| $\boldsymbol{F}$ | Flux terms | |
| $\boldsymbol{Q}$ | Vector variables, e.g. $\vec{E}, \vec{C}$ | |
| $\boldsymbol{u}$ | Scalar variables, e.g. $\phi, \rho$ | |
| $D$ | Ion diffusivity in air | $\frac{\mathrm{m}^2}{\mathrm{s}}$ |
| $T$ | Temperature | K |

# Bibliography


[1] K. Adamiak. Numerical models in simulating wire-plate electrostatic precipitators: A review. *Journal of Electrostatics*, 71(4):673–680, August 2013.

[2] Douglas N. Arnold, Franco Brezzi, Bernardo Cockburn, and L. Donatella Marini. Unified analysis of discontinuous garlerkin methods for elliptic problems. *SIAM J. Numer. Anal.*, 39(5):1749–79, 2002.

[3] J. A. Bittencourt. *Fundamentals of Plasma Physics*. Springer, 3rd edition, 2010. ISBN 978-1-4419-1930-4.

[4] Davide Cagnoni, Francesco Agostini, Thomas Christen, Nicola Parolini, Ivica Stevanović, and Carlo de Falco. Multiphysics simulation of corona discharge induced ionic wind. *Journal of Applied Physics*, 114(23):233301, 2013.

[5] Junhong Chen and Jane H. Davidson. Ozone Production in the Positive DC Corona Discharge: Model and Comparison to Experiments. *Plasma Chemistry and Plasma Processing*, 22(4):495–522, 2002.

[6] E. A. Christenson and P. S. Moller. Ion-neutral propulsion in atmospheric media. *AIAA Journal*, 5(10):1768–1773, Oct 1967.

[7] Bernardo Cockburn, Jayadeep Gopalakrishnan, and Raytcho Lazarov. Unified Hybridization of Discontinuous Galerkin, Mixed, and Continuous Galerkin Methods for Second Order Elliptic Problems. *SIAM Journal on Numerical Analysis*, 47(2):1319–1365, Jan 2009.

[8] Dorian F. Colas, Antoine Ferret, David Z. Pai, Deanna A. Lacoste, and Christophe O. Laux. Ionic wind generation by a wire-cylinder-plate corona discharge in air at atmospheric pressure. *Journal of Applied Physics*, 108(10):103306, 2010.

[9] J. L. Davis and J. F. Hoburg. HVDC transmission line computations using finite element and characteristics methods. *Journal of Electrostatics*, 18(1):1–22, Feb 1986.

[10] James L. Davis and James F. Hoburg. Wire-duct precipitator field and charge computation using finite element and characteristics methods. *Journal of Electrostatics*, 14(2):187–199, Aug 1983.

[11] Erwin Fehlberg. Low-order Classical Runge-Kutta Formulas with Stepsize Control and their Application to Some Heat Transfer Problems. NASA Technical Report NASA TR R-315, NASA, July 1969.

[12] James Q. Feng. An analysis of corona currents between two concentric cylindrical electrodes. *Journal of Electrostatics*, 46(1):37–48, Mar 1999.

[13] James Q. Feng. Application of Galerkin Finite-Element Method with Newton Iterations in Computing Steady-State Solutions of Unipolar Charge Currents in Corona Devices. *Journal of Computational Physics*, 151(2):969–989, May 1999.

[14] James Q. Feng. Electrohydrodynamic flow associated with unipolar charge current due to corona discharge from a wire enclosed in a rectangular shield. *Journal of Applied Physics*, 86(5):2412, 1999.

[15] James Q. Feng. Application of Galerkin finite-element computations in studying electrohydrodynamic problems. *Journal of Electrostatics*, 51-52:590–596, May 2001.

[16] Christopher K. Gilmore and Steven R. H. Barrett. Electrohydrodynamic thrust density using positive corona-induced ionic winds for in-atmosphere propulsion. *Proceedings of the Royal Society of London A: Mathematical, Physical and Engineering Sciences*, 471(2175), 2015.

[17] M. Goldman, A. Goldman, and R. S. Sigmond. The corona discharge, its properties and specific uses. *Pure and Applied Chemistry*, 57(9):1353–1362, 1985.

[18] S. Güzey, B. Cockburn, and H. Stolarski. The embedded discontinuous Galerkin methods: application to linear shells problems. *Int. J. Numer. Methods Eng.*, 70(7):757790, May 2007.

[19] David Halliday, Robert Resnick, and Jearl Walker. *Fundamentals of Physics.* John Wiley & Sons, Inc., 4 edition, 1993.

[20] Michael T. Heath. *Scientific Computing: An Introductory Survey.* McGraw-Hill, 2nd edition, 2002.

[21] L. G. Hector and H. L. Schultz. The Dielectric Constant of Air at Radiofrequencies. *Journal of Applied Physics*, 7(4):133–136, Nov 1936.

[22] T.J.R Hughes, G. Scovazzi, P.B. Bochev, and A. Buffa. A multiscale discontinuous Galerkin method with the computational structure of a continuous Galerkin method. *Comput. Methods Appl. Mech. Eng.*, 195(19-22):2761–2787, April 2006.

[23] N. A. Kaptsov. Elektricheskie yavleniya v gazakh i vakuume. Technical report, OGIZ, Moscow, Russia, 1947.

[24] Pijush K. Kundu and Ira M. Cohen. *Fluid Mechanics.* Elsevier Inc., 4 edition, 2008.

[25] Irving Langmuir and Katharine B. Blodgett. Currents Limited by Space Charge between Coaxial Cylinders. *Phys. Rev.*, 22:347–356, Oct 1923.

[26] L. Leger, E. Moreau, and G.G. Touchard. Effect of a DC corona electrical discharge on the airflow along a flat plate. *IEEE Trans. on Ind. Applicat.*, 38(6):1478–1485, Nov 2002.

[27] Alexandre A. Martins. Modelling of an improved positive corona thruster and actuator. *Journal of Electrostatics*, 71(1):61–67, Feb 2013.

[28] Alexandre A. Martins and Mario J. Pinheiro. Modeling of an EHD corona flow in nitrogen gas using an asymmetric capacitor for propulsion. *Journal of Electrostatics*, 69(2):133–138, Apr 2011.

[29] Kento Masuyama. Performance Characterization of Electrohydrodynamic Propulsion Devices. Master of science, Massachusetts Institute of Technology, September 2012.

[30] Kento Masuyama and Steven R. H. Barrett. On the performance of electrohydrodynamic propulsion. *Proceedings of the Royal Society of London A: Mathematical, Physical and Engineering Sciences*, 469(2154), 2013.

[31] J R Melcher and G I Taylor. Electrohydrodynamics: A Review of the Role of Interfacial Shear Stresses. *Annual Review of Fluid Mechanics*, 1(1):111–146, 1969.

[32] James R. Melcher. *Continuum Electromechanics.* MIT Press, 1981.

[33] Eric Moreau, Nicolas Benard, Jean-Daniel Lan-Sun-Luk, and Jean-Pierre Chabriat. Electrohydrodynamic force produced by a wire-to-cylinder dc corona discharge in air at atmospheric pressure. *Journal of Physics D: Applied Physics*, 46(47):475204, 2013.

[34] N. Nandakumaran and S.R.H. Hoole. Tackling Inhomogeneous Open Boundary Designs by the Finite-Element Method. *IEEE Trans. Magn.*, 44(3):360–364, Mar 2008.

[35] Namir Neimarlija, I. Demirdžić, and S. Muzaferija. Numerical Method for Calculation of Two-Phase Electrohydrodynamic Flows in Electrostatic Precipitators. *Numerical Heat Transfer, Part A: Applications*, 59(5):321–348, Feb 2011.

[36] N.C. Nguyen and J. Peraire. Hybridizable discontinuous Galerkin methods for partial differential equations in continuum mechanics. *Journal of Computational Physics*, 231(18):5955–5988, Jul 2012.

[37] N.C. Nguyen, J. Peraire, and B. Cockburn. An implicit high-order hybridizable discontinuous Galerkin method for linear convection-diffusion equations. *Journal of Computational Physics*, 228(9):3232–3254, May 2009.

[38] N.C. Nguyen, J. Peraire, and B. Cockburn. An implicit high-order hybridizable discontinuous Galerkin method for nonlinear convection-diffusion equations. *Journal of Computational Physics*, 228(23):8841–8855, Dec 2009.

[39] N.C. Nguyen, J. Peraire, and B. Cockburn. An implicit high-order hybridizable discontinuous Galerkin method for the incompressible Navier-Stokes equations. *Journal of Computational Physics*, 230(4):1147–1170, Feb 2011.

[40] N.C. Nguyen, J. Peraire, and B. Cockburn. Hybridizable discontinuous Galerkin methods for the time-harmonic Maxwell's equations. *Journal of Computational Physics*, 230(19):7151–7175, Aug 2011.

[41] F. W. Peek. *Dielectric Phenomena in High Voltage Engineering.* McGraw-Hill, New York, 1929.

[42] L. Pekker and M. Young. Model of Ideal Electrohydrodynamic Thruster. *Journal of Propulsion and Power*, 27(4):786–792, Jul 2011.

[43] J. Peraire and P.-O. Persson. The Compact Discontinuous Galerkin (CDG) Method for Elliptic Problems. *SIAM Journal on Scientific Computing*, 30(4):18061824, Jan 2008.

[44] P.-O. Persson and Gilbert Strang. A Simple Mesh Generator in MATLAB. *SIAM Review*, 46(2), 2004.

[45] Tao Shao, V.F. Tarasenk, Cheng Zhang, D.V. Rybka, I.D. Kostyrya, A.V. Kozyrev, Ping Yan, and V. Yu Kozhevnikov. Runaway electrons and x-rays from a corona discharge in atmospheric pressure air. *New Journal of Physics*, 13:113035, November 2011.

[46] P. Silvester and M.S Hsieh. Exterior finite solution for 2-dimensional exterior field problems. *Proc. IEE*, 118(12):1743–1747, Dec 1971.

[47] P.P. Silvester, D.A. Lowther, C.J. Carpenter, and E.A. Wyatt. Exterior finite elements for 2-dimensional field problems with open boundaries. *Electrical Engineers, Proceedings of the Institution of*, 124(12):1267–1270, Dec 1977.

[48] G. Skodras, S.P. Kaldis, D. Sofialidis, O. Faltsi, P. Grammelis, and G.P. Sakellaropoulos. Particulate removal via electrostatic precipitators - CFD simulation. *Fuel Processing Technology*, 87(7):623–631, Jul 2006.

[49] A. M. Tyndall and G. C. Grindley. The Mobility of Ions in Air. Part I. Negative Ions in Moist Air. *Proceedings of the Royal Society of London A: Mathematical, Physical and Engineering Sciences*, 110(754):341–358, 1926.

[50] P.A. Vázquez and A. Castellanos. Numerical simulation of EHD flows using Discontinuous Galerkin Finite Element methods. *Computers & Fluids*, 84(0):270–278, Jun 2013.

[51] Jack Wilson. An Investigation of Ionic Wind Propulsion. Technical Report NASA/TM-2009-215822, NASA, 2009.

[52] L. Zhao and K. Adamiak. EHD flow in air produced by electric corona discharge in pin-plate configuration. *Journal of Electrostatics*, 63(3-4):337–350, Mar 2005.

[53] Lin Zhao and Kazimierz Adamiak. Numerical Simulation of the Electrohydrodynamic Flow in a Single Wire-Plate Electrostatic Precipitator. *IEEE Trans. on Ind. Applicat.*, 44(3):683691, 2008.